NASA/TP—2012–216485

Risk Assessment and scaling for the SLS LOx ET

Viatcheslav (Slava) Osipov
Halyna Hafiychuk
Ekaterina Ponizovskaya-Devine
Michael Khasin,
Vadim Smelyanskiy
Ames Research Center, Moffett Field, California

December 2012

NASA STI Program ... in Profile

Since its founding, NASA has been dedicated to the advancement of aeronautics and space science. The NASA scientific and technical information (STI) program plays a key part in helping NASA maintain this important role.

The NASA STI program operates under the auspices of the Agency Chief Information Officer. It collects, organizes, provides for archiving, and disseminates NASA's STI. The NASA STI program provides access to the NASA Aeronautics and Space Database and its public interface, the NASA Technical Reports Server, thus providing one of the largest collections of aeronautical and space science STI in the world. Results are published in both non-NASA channels and by NASA in the NASA STI Report Series, which includes the following report types:

- TECHNICAL PUBLICATION. Reports of completed research or a major significant phase of research that present the results of NASA Programs and include extensive data or theoretical analysis. Includes compilations of significant scientific and technical data and information deemed to be of continuing reference value. NASA counterpart of peer-reviewed formal professional papers but has less stringent limitations on manuscript length and extent of graphic presentations.

- TECHNICAL MEMORANDUM. Scientific and technical findings that are preliminary or of specialized interest, e.g., quick release reports, working papers, and bibliographies that contain minimal annotation. Does not contain extensive analysis.

- CONTRACTOR REPORT. Scientific and technical findings by NASA-sponsored contractors and grantees.

- CONFERENCE PUBLICATION. Collected papers from scientific and technical conferences, symposia, seminars, or other meetings sponsored or co-sponsored by NASA.

- SPECIAL PUBLICATION. Scientific, technical, or historical information from NASA programs, projects, and missions, often concerned with subjects having substantial public interest.

- TECHNICAL TRANSLATION. English-language translations of foreign scientific and technical material pertinent to NASA's mission.

Specialized services also include organizing and publishing research results, distributing specialized research announcements and feeds, providing information desk and personal search support, and enabling data exchange services.

For more information about the NASA STI program, see the following:

- Access the NASA STI program home page at http://www.sti.nasa.gov

- E-mail your question to help@sti.nasa.gov

- Fax your question to the NASA STI Information Desk at 443-757-5803

- Phone the NASA STI Information Desk at 443-757-5802

- Write to:
  STI Information Desk
  NASA Center for AeroSpace Information
  7115 Standard Drive
  Hanover, MD 21076-1320

NASA/TP—2012–216485

Risk Assessment and scaling for the SLS LOx ET

Viatcheslav (Slava) Osipov
Halyna Hafiychuk
Ekaterina Ponizovskaya-Devine
Michael Khasin,
Vadim Smelyanskiy
Ames Research Center, Moffett Field, California

National Aeronautics and
Space Administration

Ames Research Center
Moffett Field, CA 94035-1000

December 2012

Acknowledgments

Available from:

NASA Center for AeroSpace Information
7115 Standard Drive
Hanover, MD 21076-1320
443-757-5802

ABSTRACT

In this report we analyze the transpiration cooling by He bubble injection of the long LOx tank feedline heated by the environment heat. We consider possible hazards that can arise in the proposed design of the SLS core stage where the feedline length is much longer than that used in the Space Shuttle.

CONTENT

Nomenclature

ρ	= density
p	= pressure
p_c	= critical pressure for gas
T	= temperature
T_c	= critical temperature for gas
T_s	= surface or interface temperature
u	= velocity
c	= sound velocity
M	= Mach number, $M = u/c$, $M_0 = u/c_0$
C_V	= specific heat for the constant volume
C_P	= specific heat for the constant pressure
γ	= ration of specific heats; $\gamma = c_p/c_V$
g	= gravity
R_t	= radius
S_t	= radius of tank
Ssu	= surface of tank cross-section
r	= total surface of tank
L_D	= thermodiffusion length
q_L	= heat of evaporation
h_T	= heat transfer coefficient
j	= mass flow density [$j = u\rho$]
J	= mass flow [$J = u\rho S$]
q	= heat flow density
Q	= heat flow
Q_c	= convection heat flow
Q_R	= radiation heat flow
β_T	= thermal expansion coefficient
δ	= boundary layer thickness
k	= thermal conductivity
v	= kinematic viscosity
μ	= dynamical viscosity
Pr	= Prandtl number, $Pr = \mu C_p/k$
Ra	= Raleigh number
Re_x	= Reynolds number
Gr	= Grashof number
Nu	= Nusselt number

Subscripts:

g	= gas
L	= liquid
env	= environment
t	= tank
w	= tank wall
ull	= ullage
eva	= evaporation
p	=condensation
con	
d	

Abbreviations:

LH2	= Liquid Hydrogen
GH2	= Gaseous Hydrogen
MNM	= Multinode Model
SLS	= Space Launch System
3D	= Three dimensional

Introduction

Here we study main physical processes taking place in LOx tank during the pre-pressurization stage and the rocket flight. The goal of this research is to analyze the risks associated with the functioning of the external LOx tank of the Space Shuttle (Fig.1) during the pre-pressurization and in the course of the flight and their scaling to the proposed SLS design with 5 engines (the situation with 4 engines is less critical). The risk assessment for the replenish stage is presented in a separate report.

We use both the protocol [1] and the telemetric data [2] for Shuttle flights to fit an uncertain parameter of the multinodes model (MNM) developed in our group using results of

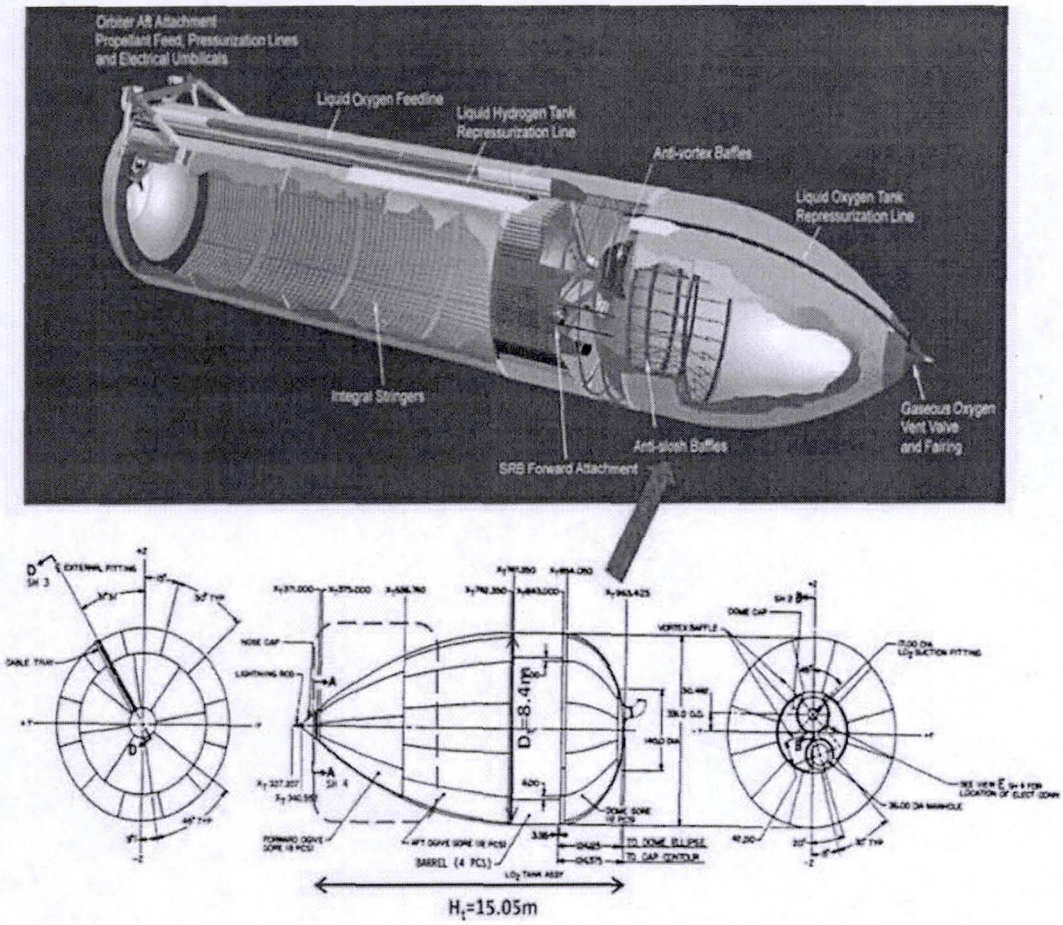

Fig.1. Design of the Shuttle tanks: the shape and parameters of the LOx tank

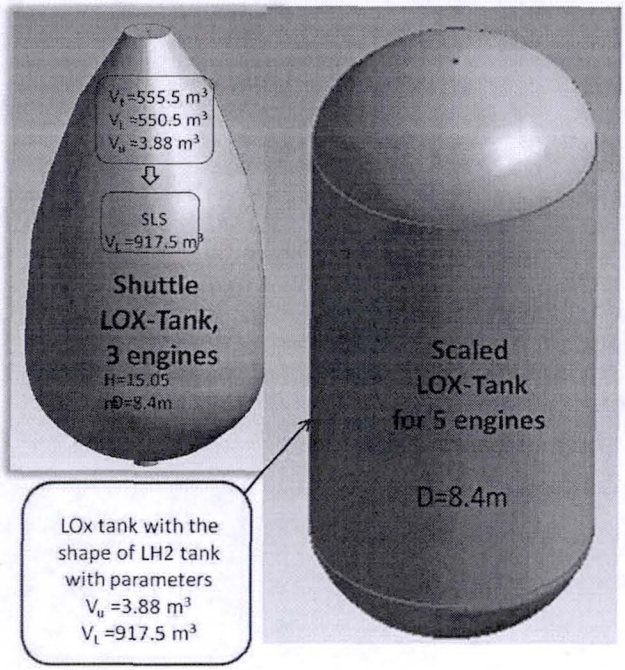

Fig.2. The shapes of the LOx tanks analyzed in this work

works [3-5]. After an appropriate rescaling the model is further applied to study the temperature stratification, the ullage pressure dynamics and the associated risks in the LOx tank in the framework of the proposed SLS designs. This constitutes the risk scaling problem. Two different designs of the LOx tank will be considered. The first is tank of the shape of LOx Shuttle tank (Fig.1), but with elongated central part to contain 5/3 of the Shuttle tank LOx volume (Figure 2, left). The second is tank of the shape of LH2 tank of the Shuttle, rescaled to contain 5/3 of the Shuttle tank LOx volume (Figure 2, right).

1. Main physical processes and pathways of heat transfer in the LOx tank

The general heat balance in the LOx tank can be written as

$$Q_{inject} + Q_{env} = Q_{ullage} + Q_{wall} + Q_L. \quad (1)$$

Here $Q_{inject} + Q_{env}$ is the total heat added to the tank as a result of hot gas injection from the diffuser and the interaction with environment. This heat is spent on heating the gas in the ullage, Q_{ullage}, heating the tank wall, Q_{wall}, and on condensation-evaporation processes including heating of the surface layer of the liquid , Q_L. The heat flows associated with these pathways are sketched in Fig. 1, which also defines the variables of the physical model.

We now proceed to analyzing these pathways and estimating their relative importance for the problem of temperature stratification and pressure dynamics in the ullage.

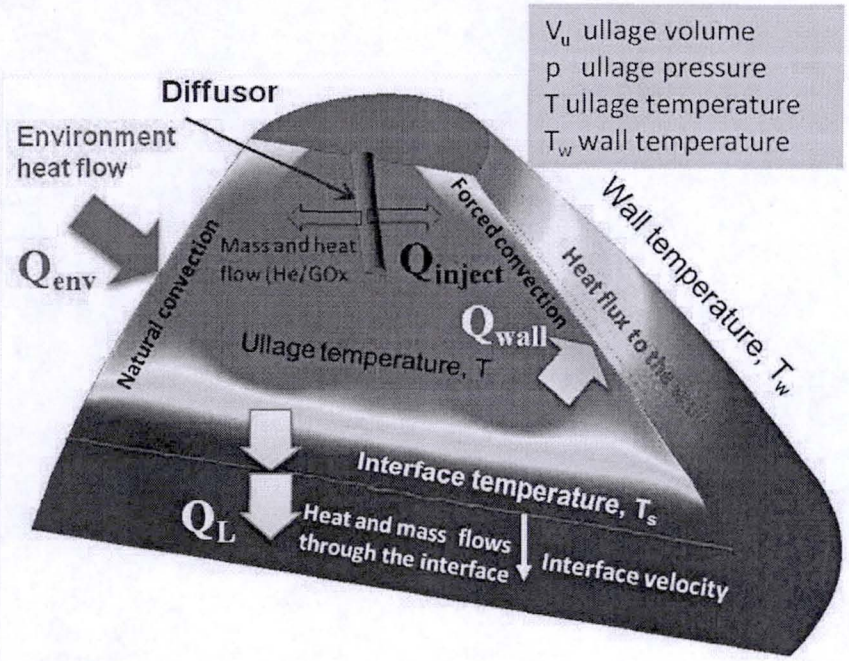

Fig.1-1. Main physical processes, variables and pathways of heat transfer.

1.1. Condensation-evaporation processes

The timescale of the ullage pressure changes is large (~1 sec) compared to the timescale of thermalization of the liquid-vapor interface, which can be estimated as follows [6]:

$$\tau_{thermo} = \left(2\pi^2 \kappa_L C_L \rho_L R_{vapor} T_L^3\right) / \left(p_{sL}^2(T_L) q_h^2\right) < 0.1 m\sec \qquad (2)$$

Here $\rho_{L,g}, C_{L,g}, \kappa_{L,g}$ are density, heat capacity, and thermo-conductivity of liquid (vapor); R_{vapor}- gas constant; q_L - heat of vaporization. As a consequence, the quasi-equilibrium near the interface can be assumed for all times with the surface temperature T_s determined by the vapor pressure $p_{vapour} = p_{GOx}$ [6,7]:

$$T_s = T_c \left(\frac{p_{GOx}}{p_c}\right)^{1/\lambda}, \quad p_s(T) = p_c \left(\frac{T}{T_c}\right)^{\lambda}. \qquad (3)$$

Here T_c and p_c are the critical temperature and pressure of the gas, p_s is the pressure of the saturated vapour and the constant λ=7.2 for oxygen [7]. Note, that p_s=1atm at T=T_L=90K, during of the prepress and flight p_{GOx}>1atm and $T_s > T_L$ ($T_s(p_{GOx}$=2.25atm=36psi)=100K > T_L =90K). The mass flow at the interface is limited by the heat balance between the hot gas and the cold liquid surface. In what follows we analyze the condensation-evaporation processes during the pre-pressurization. Condensation-evaporation during flight is discussed in Section 3.

The condensation of GOx prevails over the evaporation during the first stage of pre-pressurization (Fig.1-2, -152s < t < -138sec). This result can be understood as follows. In the beginning of He injection (t= -152sec, see Section 2) the Ox vapor is compressed toward the liquid-gas interface due to the relatively high density of GOx. As a consequence the partial pressure of GOx increases (Fig. 1-3).

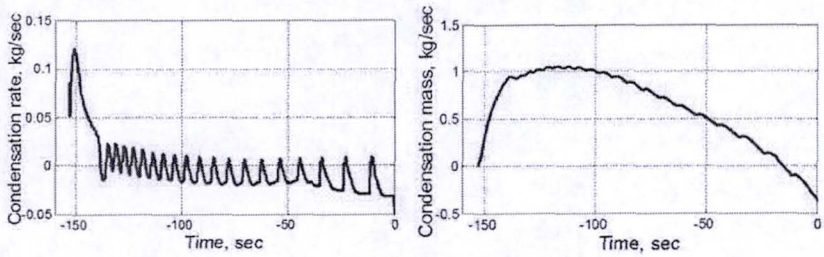

Fig.1-2. GOx condensation mass flow and total condensed mass. Results of MNM simulation.

Accordingly, the condensed mass accumulates at this stage and reaches the maximal value of ~1kg which supports the estimations presented in the text. At the later stage (-138 sec <t<0 sec) the condensation rate is seen to oscillate due to the pressure modulations and decreases on average as predicted. The average condensed mass decreases at this stage.

The 3D simulations confirm this conclusion (Fig.1-4). The growth of the GOx partial pressure stimulates condensation of the compressed GOx, accompanied by the rise of surface temperature

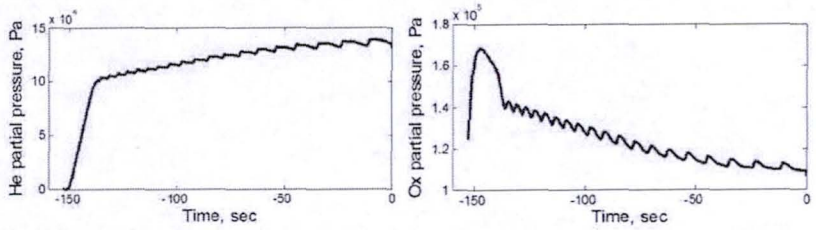

Fig.1-3: Partial pressure dynamics of GOx and GHe during the pre-pressurization in the ullage layer near the liquid-gas interface. Results of MNM simulation.

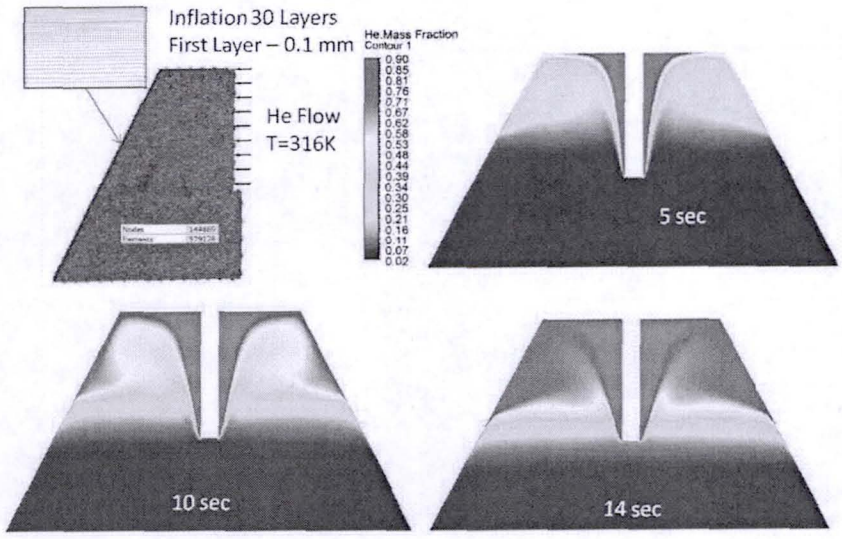

Fig.1-4. Stratification mass fraction of GOx and He during the pre-pressurization

in accordance with Eqs. (2). The liquid surface temperature T_s is determined by the partial pressure p_{GOx} of Ox vapor near the interface: $T_s > T_L$ at $p_{GOx} \approx$ 1.75atm > p_s(T)=1atm, where T_L is the liquid temperature far from the interface. The temperature profile near the interface and the heat flows are schematically shown on Fig. 1-5.

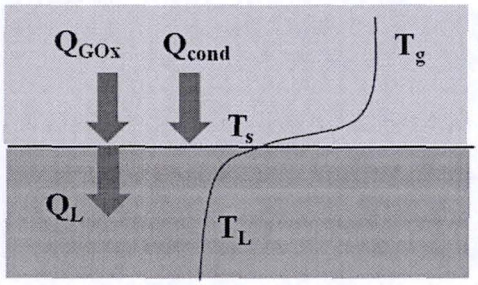

Fig.1-5: Temperature profile near the liquid-gas interface

Since $T_s > T_L$ and $T_g > T_s$ the convection of both the liquid and the vapor is absent. Moreover, our simulations have also shown that the convection induced by the hot gas injection from the diffuser and natural convection near the wall is indeed very small near the gas-liquid interface. Thus, the heat balance in condensation-evaporation processes is established mainly by means of thermo-diffusion for the given surface temperature $T_s(p_{GOx})$. The solution of the one-dimensional heat equation

$$C_{L,g}\rho_{L,g}\frac{\partial T}{\partial t} = \kappa_{L,g}\frac{\partial^2 T}{\partial x^2}, \tag{4}$$

for the boundary condition $T(0,t) = T_s = const,\ T(x,\infty) = T_L$ is given by

$$T(x,t) = T_L + (T_s - T_L)erf\left(\sqrt{\frac{C_{L,g}\rho_{L,g}x^2}{4\kappa_{L,g}t}}\right) \tag{5}$$

Here $\rho_{L,g}, C_{L,g}, \kappa_{L,g}$ are density, heat capacity, and thermo-conductivity of liquid (vapor); x=0 corresponds to the liquid-vapor interface, and erf is the error function. Using Eq. (5) we can find the heat flux from the warm interface into the liquid:

$$\dot{Q}_L(x,t) = -\kappa_L\left.\frac{\partial T(x,t)}{\partial x}\right|_{x=0} = -\kappa_L\frac{T_s - T_L}{L_{DL}} = -\sqrt{\frac{C_L\rho_L\kappa_L(T_s - T_L)^2}{\pi t}},\quad L_{DL} = \sqrt{\frac{\pi\kappa_L t}{C_L\rho_L}}. \tag{6}$$

Here L_{DL} is characteristic thermo-diffusion length in the liquid. This makes it possible to estimate the condensation mass flow j_{cond} from the following balance equation:

$$\dot{Q}_{cond} = j_{cond}(t)S_L\left(q_L + C_{GOx}(T_g - T_s)\right) = \dot{Q}_L - \dot{Q}_g = S_L\left(\frac{T_s - T_L}{L_{DL}(t)} - K_g\frac{T_g - T_s}{L_{Dg}(t)}\right),$$
$$j_{cond}(t) = \frac{\sqrt{K_L C_L \rho_L}(T_s - T_L) - \sqrt{K_{GOx}C_{GOx}\rho_{GOx}}(T_g - T_s)}{\sqrt{\pi}\left(q_L + C_{GOx}(T_g - T_s)\right)} \tag{7}$$

The first term in the left-hand side of Eq. (7) describes the condensation flow rate and the second one describes the evaporation flow rate. The total mass of the condensed vapor is given by

$$M_{cond}(t) = \int_0^t S_L(t) j_{cond}(t) dt, \quad M_{cond}(t) \propto \sqrt{t} \text{ at } S_L(t) \approx const \tag{8}$$

According to Eq. (7) condensation will be dominant whenever

$$\left(T_g - T_s(p_{GOx})\right) < \left(T_s(p_{GOx}) - T_L\right) \sqrt{\frac{K_L C_L \rho_L}{K_{GOx} C_{GOx} \rho_{GOx}}}, \; T_s(p_{GOx}) = T_c \left(\frac{p_{GOx}}{p_c} \right)^{1/7} \tag{9}$$

where for the estimation of the thermo-diffusion length in the gas we can use parameters of the pure Ox, which is prevalent in the vicinity of the interface as argued above. We note that Eqs. (7)-(9) are valid during the flight as well (see Section 3).

At the early stage of the pre-pressurization, condition (9) is satisfied. As argued above, the partial pressure of the compressed GOx vapor is controlled by the pressure of the injected He, $p_{GOx} \approx 1.75 atmi$ during the early stage of pre-pressurization (Fig.1-3). In this case the surface temperature $T_s(p=1.75)=97.5 > T_L = 90K$ and the condition (9) holds provided $T_g < 450K$, which is certainly satisfied (temperature of injected He is 320K). Estimation [Eq. (8)] of the total condensed mass during the early stage of pre-pressurization (~14sec) gives $M_{cond} \approx 1kg$. This estimate is supported by the results of the simulation (Fig. 1-2). Since the initial mass of the vapor is $M_{GOx} = \rho_{s,Ox} V_{\text{ullage}} = 17\text{kg}$ and the mass of injected He is about 6kg, the condensed mass constitutes about 4% of the total mass of the gas in the ullage. (We note that the mass fraction of the gas involved in the condensation-evaporation is considerably smaller during the flight, see Sec.3).

At the later stage of pre-pressurization (-138sec < t < 0) the vapor becomes mixed with hot He and the GOx partial pressure will drop (Fig.1-3). The gas temperature near the interface T_g~100K (Fig. 1-6). Therefore, at this stage the condensed mass decrease. The foregoing theoretical predictions are verified by the results of MNM simulation plotted in Figs.1-3 and 1-6.

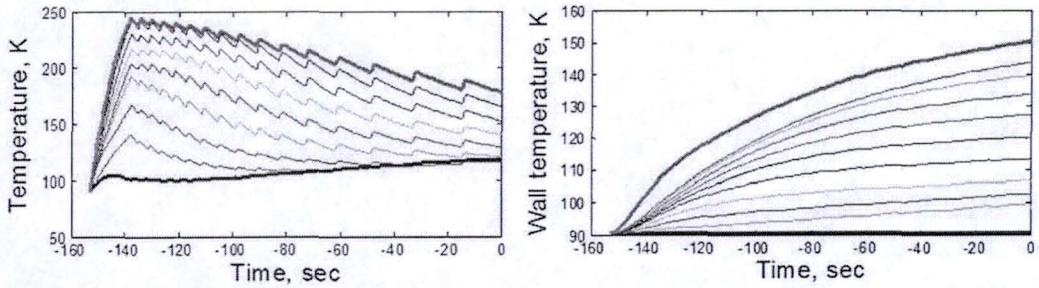

Fig.1-6. Ullage and wall temperature during the pre-pressurization: upper red and blue curves for the layers near top and bottom of the tank, respectively. Results of the MNM simulation.

We note that at the later stage of pre-pressurization weak modulations of the partial pressure of GOx (Figure 1-3) are observed in Fig.(1-3). These modulations are due to pulsations in the hot He injection from the diffuser (see Section 2). The pulsations have been neglected in our estimations but the average decrease of the partial LOx pressure in the vicinity of the interface supports the theoretical argument. The average decrease of the partial pressure is accompanied by the decrease of the surface temperature (Fig. 1-6) which displays modulations as well.

The condensation-evaporation during the flight is discussed in Section 3.

1.2. Collapsing of bubbles during the initial stage of the pre-pressurization

Ullage pressure increases from 1atm to 2.45atm during the pre-pressurization (-152sec <t< -138sec) due to injection of GHe. Therefore, the LOx becomes strongly overcooled and the bubbles which can be present in the liquid start to collapse. The characteristic time of collapsing can be estimated from the following heat balance equation

$$-S_{bubble}K_L\frac{\left(T_{s,bubble}-T_L\right)}{r_{bubble}}dt = S_{bubble}\rho_{s,Ox}q_L dr_{bubble},$$
$$r^2_{bubble}(t) = r^2_{bubble,0}(1-\frac{t}{t_{collaps}}),\ t_{collaps} = \frac{r^2_{bubble,0}\rho_{s,Ox}q_L}{2K_L\left(T_{s,bubble}-T_L\right)} \quad (10)$$

Here $T_{s,bub}$ is bubble surface temperature that is determined by the ullage pressure

$$T_{s,bubble} = T_c\left(\frac{p_{ullage}}{p_c}\right)^{1/7.3},\ t_{collapse} = 0.2\sec\left(\frac{r_{bubble,o}}{1mm}\right)^2,$$
$$t_{collapse} = 1.25(5)\sec\ at\ r_{bubble,o} = 2.5(5)mm. \quad (11)$$

Here we took into account that p_{ullage}= *2.45 atm* during the pre-pressurization (-138sec<t<0). Then, $T_{s,bubble}$ =102K and the density of saturated vapour in the bubbles is $\rho_{s,Ox} = 3.48kg/m^3$. Validity of estimations given by Eq. (10) was confirmed by numerical simulations based on a more elaborate model of bubbles' collapsing in overcooled liquids [8]. Duration of the pre-press is longer than 100sec. Thus, all bubbles are expected to collapse by the start time t=0.

1.3. Heating of liquid in the boundary layer near the interface

The liquid surface layer is heated due to condensation. It can see from Fig. 1-3 the partial GOx pressure near the interface p_{GOx}<1.7atm. Therefore, the surface temperature of the liquid according to Eq. (3) is $T_s \le 97K$ (T_s-$T_L \le 0.7K$). The width of this warm liquid layer near the gas-liquid interface is determined by the thermodiffusion length of the liquid which increases with time and approaches a value of $L_{DL} = 6mm$ toward the end of the flight.

The upper bound on the mass of heated liquid can be estimated as $M_{\max} \approx S(t_{flight})\rho_L L_{DL}(t_{flight}) \approx 400kg$. This value is negligible compared to the total LOx mass in the filled tank, 627,500kg.

The heat flux into the liquid associated with the condensation is given by

$$\dot{Q}_L - \frac{dQ_L}{dt} = K_L\frac{(T_s-T_L)}{L_{DL}(t)}S_L(t) = (T_s-T_L)S_L(t)\sqrt{\frac{K_L C_L\rho_L}{\pi t}} \quad (12)$$

The total heat associated with the condensation of GOx can be estimated as

$$Q_L(t) \approx 2(T_s-T_L)\bar{S}_L\sqrt{t\ K_L C_L\rho_L/\pi},\quad Q_L(t_{\text{flight}}) \approx 10^7 J \quad (13)$$

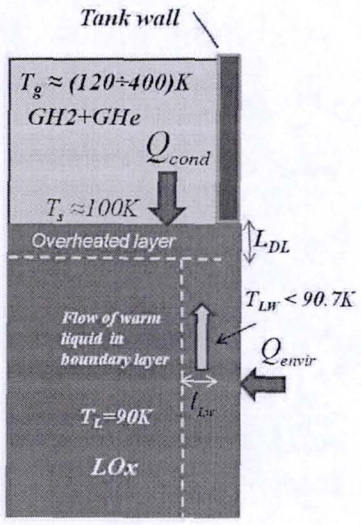

Fig. 1-6: Heated layers near the interface and the tank wall

The total heat of GOx injected during the flight (t_{flight} =500sec) is

$$Q_{inject} = C_{pOx} T_{inj} J_{inj} t_{flight} = 3.4 \cdot 10^8 J,$$

$$Q_{ullage} = C_{pOx} M_{GOX} T_{ullage} = C_{pOx} \frac{p_{ullage} V_{\text{tank}}}{R_{Gox}} = \frac{\gamma p_{ullage}(t_{flight}) V_{\text{tank}}}{\gamma - 1} = 2.45 \cdot 10^8 J \quad (14)$$

$$J_{inj} = 1.3 kg/\text{sec},\ T_{inj} = 800R = 444K$$

We conclude that the relative heat content of the heated liquid layer is a small: $Q_L(t_{flight}) / Q_{inject} = 3\%$.

1.4. Heating of liquid in the boundary layer near the wall

Heating of LOx near the tank wall occurs due to the environmental heat flux, $\dot{Q}_{envir} = \dot{q}_{envir} S_{\text{tank}}$ which causes free convection of the liquid near the wall. The convection flow is turbulent and can be described by the following relations, discussed in a separate report:

$$\dot{q}_{envir} - \frac{dq_{envir}}{dt} = h(T_{LW} - T_L) = K_L \frac{(T_{LW} - T_L)}{l_{Lw}},\quad h_{Lw} = 0.15 K_L \frac{(Ra_x)^{1/3}}{x},$$

$$Ra_x = \frac{g\beta_T C_L \rho_L (T_{LW} - T_L) x^3}{\mu_L K_L},\quad l_{Lw} = \frac{x}{0.15(Ra_x)^{1/3}} \approx 0.5mm \quad (15)$$

where l_{Lw} is effective thickness of the heated layer near the wall. Here we use correlations for the turbulent free convection flow as in this case Rayleigh number $Ra_x > 3x10^{12}$ for x>1m (x is the elevation of liquid layer counted from the tank bottom). We note that the values of l_{Lw} and heat transfer coefficient h_w do not depend on x. According to Eq. (15) the temperature increase of LOx layer near the wall is less than *0.7K*: $(T_{LW} - T_L) < 0.7K$ for typical environmental heat fluxes, $\dot{q}_{envir} = (130 \div 200) W/m^2$. The total mass of the slightly heated liquid in the boundary layer can be estimates as follows:

$$M_{LOx,T\approx 90.7K} \le S_{\text{tank}}\rho_L l_{Lw}, S_{\text{tank}} - \text{tank surface area},$$
$$M_{LOx,T\approx 90.7K} \le 215kg\,(360kg)\ for\ 3\,(5)\ engines. \tag{16}$$

We note that the total LOx mass in the tank is 627,500kg (1,046,000kg). Thus, the mass fraction of the heated liquid ($T_{LW} \approx 90.7K$) near the wall is negligible quantity and does not play a role in the ullage temperature stratification and pressure dynamics. Moreover, the thin warm liquid layers with T ≤ 90.7K near the interface and the tank wall, i.e. a slight stratification of LOx, does not lead to breach of condition $NPSP = p_{ull} + p_{head} - p_{fric} - p_{s,vap}(T_s) > 30psi$ for the net positive suction pressure due to high hydrostatic head pressure P_{head} (see below Sec. 5.1).

1.5. Heating of the tank wall by hot gas: main mechanism of the gas cooling

The heat flux from the ullage at T_g to the tank wall at T_w can be written as

$$\dot{q}_{gw} \equiv \frac{dq_{gw}}{dt} = h_{gw}(T_g - T_w),\ h_{gw} = \frac{0.15}{x}K_g(T_g)\left(Ra_x\right)^{1/3} \approx 20\frac{W}{m^2K},$$
$$Ra_x = \frac{g\beta_{gT}C_g\rho_g(p,T_g)(T_g - T_w)x^3}{\mu_g K_g(T_g)}, \tag{17}$$
$$l_{Lw} = \frac{K_g}{h_w} \approx 1mm\ for\ p = 2.4atm, T_g = 425K, T_w = 250K.$$

Here we use the correlation formulas for the turbulent regime corresponding to large Rayleigh number $Ra_x > 7\times 10^{13}$ for x~1m. The total heat flow is

$$\frac{dQ_{gw}}{dt} = h_{gw}(T_g - T_w)\delta S_{ull}(t) = d_w C_w(T_w)\rho_w \delta S_{ull}(t)\frac{dT_w}{dt}. \tag{18}$$

The temperature of the ullage and the tank wall depends on the coordinate x along the wall. Temperature dependences of the specific heat C_w for Al alloys used for the tank is shown in Fig.1-7.

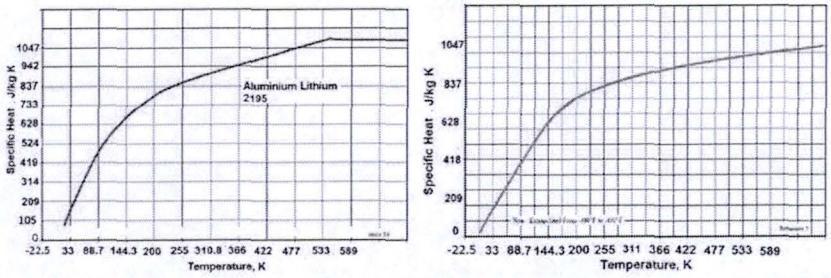

Fig. 1-7: Specific heat for Al Alloys 2195 (left) and 2219 (right)

These dependences were used for our MNM numerical simulations. For the estimation we assumed $T_g = const$, $C_w(T_w) = \langle C_w \rangle = const$ and $h_{gw} = const$. Then Eq. (18) implies

$$\frac{dT_w}{dt} = \frac{(T_g - T_w)}{\tau_{gw}(T_w)},\ T_w = T_g - (T_g - T_{w0})\exp(-\frac{t}{\tau_{gw}}),$$
$$\tau_{gw}(T_w) = \frac{\langle C_w \rangle \rho_w d_w}{h_{gw}}, \tau_{gw} \approx 150\text{sec}\ at\ \langle C_w \rangle \approx 600\text{J/kgK}. \quad (19)$$

The changes in the temperature of ullage gas and in the temperature of the tank wall are shown in Fig.1-8. The solid lines are plots of MNM-simulated time-traces of temperatures near the top (red) and bottom of the tank (green). The dashed lines are MNM-simulated time traces of the tank wall temperature near the top (red) and the gas-liquid interface of the tank (green). The blue solid lines give the estimated tank wall temperature near the tank top and the interface according to Eq.(13) for τ_{gw}=150sec. These analytical curves correspond fairly well to the results of the MNM simulation (Fig. 1-8).

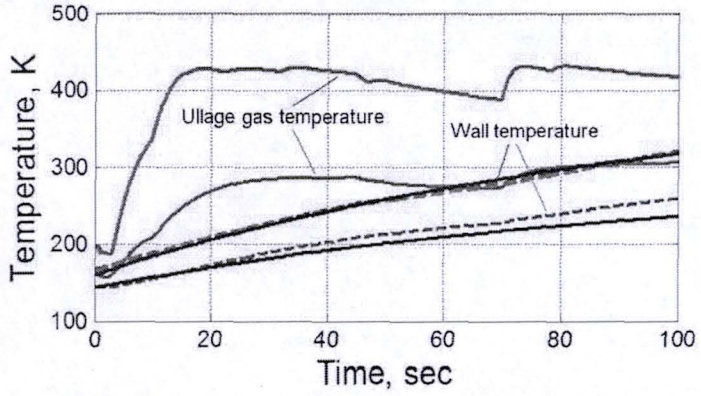

Fig. 1-8 Time traces of the ullage and wall temperature: solid curves are MNM simulation results and dashed curves are analytical results

It it follows from Eqs. (12),(13) and (14) the heat transferred from the hot gas to the tank wall is

$$Q_{wall} = Q_{inject} + Q_{env} - Q_{ullage} - Q_L \approx 6.8 \cdot 10^7 J,$$
$$Q_{inject} = C_{pOx} T_{inj} J_{inj} t_{flight} = 3.4 \cdot 10^8 J, \quad (20)$$
$$Q_{ullage} = \frac{\gamma p_{ullage}(t_{flight}) V_{\text{tank}}}{\gamma - 1} = 2.45 \cdot 10^8 J, Q_{env} = q_{env} S_{\text{tank}} t_{\text{flight}} \approx 3.7 \cdot 10^7 J$$

Thus we conclude that heating of the wall is the main mechanism of gas cooling in the ullage.

2. Pre-pressurization regime and fitting the Shuttle data

The values of main parameters at the end of replenish (EOR) and at the engine start command (EST) are shown in Table 1 (from [1]). The variation of ullage pressure during the period, t = -300sec to t = 0, is shown in Fig. 2-1 [1]. The nominal parameters of liquid and gases supply for STS -115 are presented in Table 2 [1]. The replenish stage ends at t = -300sec, i.e., 300sec before the start. The pre-pressurization starts at $t^{(0)}_{prepress} = -152.8\text{sec}$ with injection of the hot He. The nominal He flow rate is r_{He}=0.3lb/sec = 0.136kg/sec and He temperature is T= 572.4R=318K (see Table 2).

After the EOR one observes a leak of LOx which increases abruptly and reaches the rate of 18lb/s = 9.1kg/s (Fig. 2-2). Therefore, the ullage volume at $t^{(0)}_{prepress}$ can be estimated as follows:

$$V_{ul}^{(0)} = V_{ul}^{EOR} + 8.1\text{kg/s}\,\Delta t/\rho_L \simeq 5\text{m}^3, \Delta t \simeq (300-152.8)s = 157.2s$$

where the liquid level $x^{(0)}_{ul} = 1.09m$ is measured from the top of the tank downward. Hot He is supplied during the time $\Delta t^{(0)}_{prepress} = (152.8-138.8)\,\text{sec} = 14\text{sec}$ until the pressure reaches 20.54 psig=2.42atm (Fig. 2-1). At $t^{(1)}_{prepres} = -138.8\,\text{sec}$ (liquid level $x^{(0)}_{ul} = 1.406m$) the ullage volume

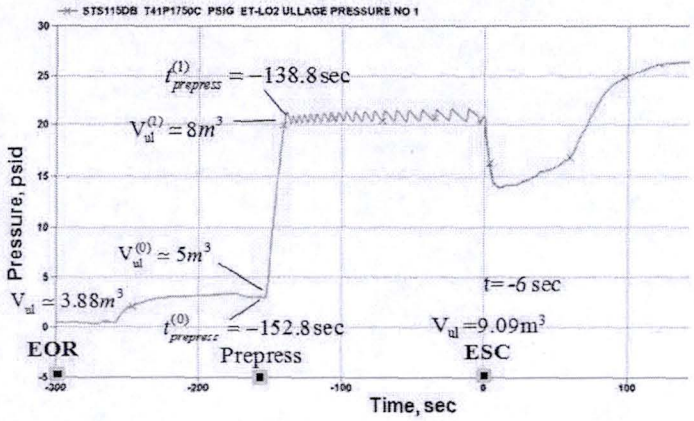

Fig. 2-1: Time-trace of the ullage pressure (STS 115).

increases to $V_{ul}^{(1)} = V_{ul}^{ESC} - 9\frac{kg}{\text{sec}} 138.8\,\text{sec}/\rho_L \simeq 8m^3$. We also used the fact that the ullage volume increases with the pressure approximately as $V_{ul}(p) = V_{ul}^{(0)} + \frac{V_{ul}^{(1)} - V_{ul}^{(0)}}{p_1 - p_0}(p - p_0)$ due to the tank wall elasticity and the lowering of LOx level.

The temperature, partial pressure and densities of GOx and He stratify at $t^{(1)}_{prepress} = -138.8\,\text{sec}$ as shown in Figs. 1-3 and 1-4 (MNM simulation) and Figs. 2-3 and 2-4 (3D simulation).

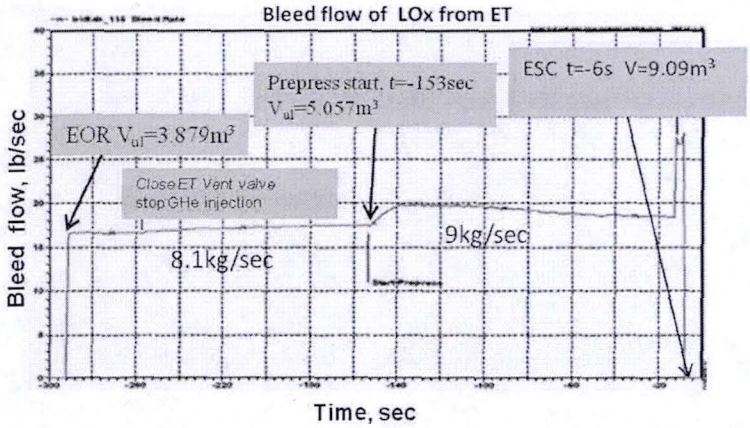

Fig. 2-2: Time-trace of leakage from LOx tank during stages EOR through ESC (STS 115).

Table 1: EOR through ESC (from t=-300sec to t=0) including pre-press (STS-115)

EOR			ESC Through T-0	
Ambient Pressure:		14.62 psia †	LO2 Losses Prior to ESC:	5,904 lb_m
Nose Cone ΔP		0.01 psi	GHe (Anti-Ice) Mass Added:	1 lb_m
Ullage Pressure: (above ref)		0.64 psid	GHe (Prepress) Mass Added:	13 lb_m
Ullage Pressure:		0.65 psig	Ullage Pressure:	22.0 psig
Ullage Pressure:		15.27 psia	Ullage Pressure:	36.62 psia
Liquid Level:		412.58 Xt	Ullage Volume @ ESC (X=1.514m)	321 ft^3 9.09m^3
Ullage Volume:	(X=0.929m) 3.879m^3	137 ft^3	Ullage Mass @ ESC	49 lb_m
Ullage Mass:		36 lb_m	ET Liquid Volume @ ESC	19,354 ft^3
Total Tank Volume:	555.51m^3	19,617 ft^3	ET Liquid Mass @ ESC	1,377,432 lb_m
Bubble Volume:	1.133m^3	40 ft^3	Press'd LO2 Density	71.17 lb_m/ft^3
Liquid Volume:	550.5m^3	19,440 ft^3	Predicted LO2 Usage to T-0:	9,530 lb_m
Vented LO2 Density:		71.16 lb_m/ft^3	LO2 Transferred to SSMEs:	172 lb_m
LO2 Propellant Load:	627.5 T	1,383,336 lb_m	Loaded LO2 at T-0:	1,367,730 lb_m
			Predicted Ullage Volume - % of Liquid Volume	1.66
			Required Ullage Volume - % of Liquid Volume	1.59

XT375 – ET top
XT396.7 – 0.5m down
XT412 – 0.95m down (initial liquid level == ullage)

The ullage pressure drops at $t \geq t^{(0)}_{prepress} > -138\,\text{sec}$ due to cooling of the hot injected He (see Sec. 1.4) and expansion of the ullage volume. Pulses of He injection are applied when the ullage pressure drops below the threshold value of p_{th} =20.54 psig=2.42atm (nominal value, Table 2). The results for the pressure time-trace from 3D simulation are presented in Fig. 2-5. Rectangular He pulses of nominal duration 0.5sec and nominal amplitude j_{He}=*0.3lb/sec=0.136kg/sec* (Table 2) were used for the simulation.

One can see from Eq. 2-5 the time-trace pressure deviates from the telemetric data during the pre-pressurization stage. This divergence is a consequence of (i) the deviation of the actual pulse shape (Fig. 2-6) from the rectangular shape and (ii) the deviation of the experimental threshold pressure p_{th} from its nominal value 20.54 psig used in the simulation. We incorporated the actual (experimental) rather than nominal value of the threshold and the actual pulse shape in the MNM simulation which shows an excellent agreement with the telemetric data (Fig. 2-7). In more detail, the pulses have amplitude j_{He}=*0.3lb/sec=0.136kg/sec* and their form is given by:

$$j(t) = j_{He}\begin{cases} 1-\exp\left(-(t-t_i)/\tau_{front}\right), & t < t_i + \tau_p \\ \exp\left(-(t-t_i-\tau_p)/\tau_{tail}\right), & t > t_i + \tau_p \end{cases} \qquad (21)$$

where at $t=t_i$ the ullage pressure drops to the threshold value of p_{th} and i-pulse is generated.

Table 2. Tank Ullage Pressure Dispersions

PARAMETER	NOMINAL VALUE			3σ VARIATION
Trajectory	Normal & Early RTLS			
SSME	#1	#2	#3	
• Pressure †	3560	3584	3579	+42.4 / -55.9 psi
• Temperature †	830	820	852	+31.9 / -39.9 °R
• Orifice Area	0.02871	0.02761	0.02944	±2%
• Nominal Power Level	104.5%	104.5%	104.5%	
• LO_2 Flowrate	933.28 lb_m/sec			+6.33 / -6.78 lb_m/sec
Ullage Volume at End of Replenish	137ft^3			±22.3 ft^3
Pre-Pressurization				
• *Transducer Accuracy*	Tavis Flight Experience			± 0.4 psi
• Drain Back / Seal Leak	21.4 lb_m/sec			± 1.5 lb_m/sec
• Max. Hold Time	0 sec			5.0 min.
He Pre-press Supply				
– Flowrate	0.3 lb_m/sec			± 0.05 lb_m/sec
– Supply Temperature	572.4°R			+ 8.7 / -19.5 °R
– Valve Open Time	0.5 sec			± 0.1 sec
Ullage Pressure at T_0	20.54 psid			+ 0.176 / - 0.348 psi
Ambient Temperature	79.75°F			48.8 / 81.6 °F
LO_2 Splash Effects				
• Splash Coefficient	4.375‡			± 0.35

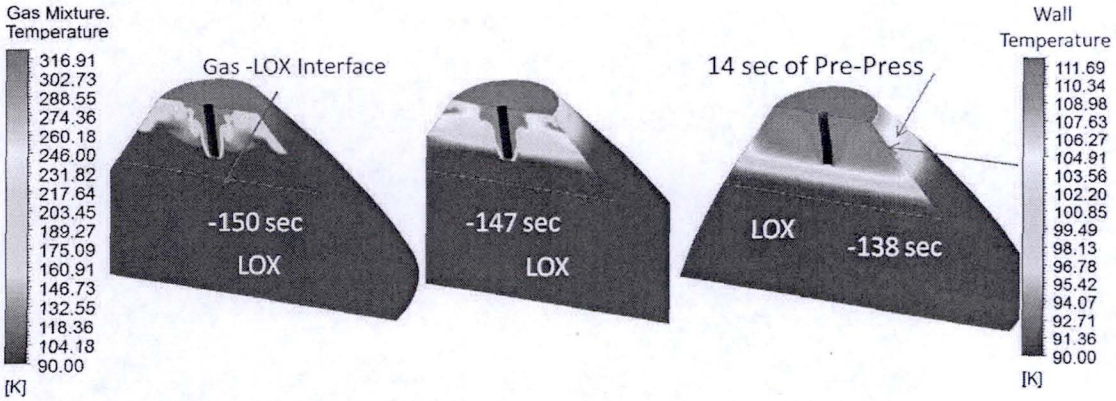

Fig. 2-3: Stratification of the ullage and wall temperature of GOx/He during the pre-pressurization. Results of 3D simulation.

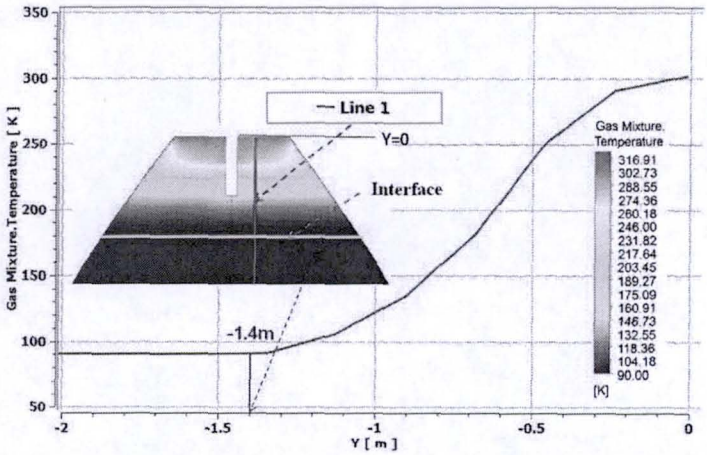

Fig. 2-4: Temperature distribution along line 1 on a tank section at $t^{(1)}_{prepress}$ = -138sec corresponding to the pressure p=2.42atm (see Fig. 2-5). Results of the 3D simulation.

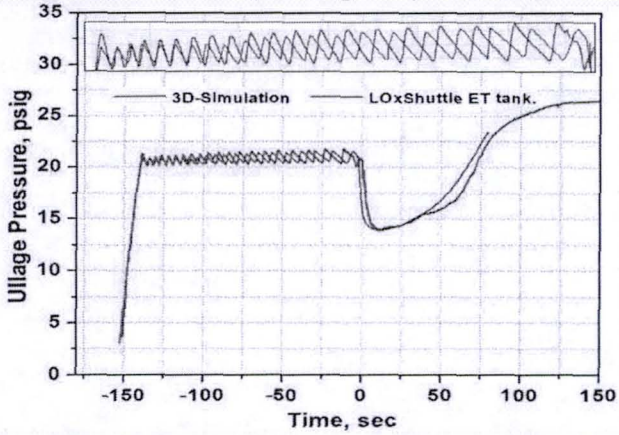

Fig.2-5: Ullage pressure during the pre-pressurization and the first part of the flight: STS115DB telemetry (red) and 3D simulation (blue).

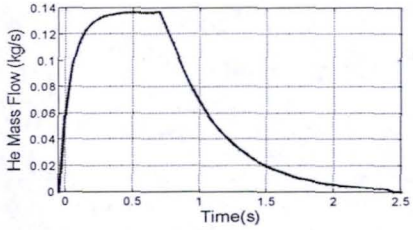

Fig. 2-6: The form of the He mass flow pulses.

We chose a single fitting parameter of MNM, numerical coefficients β_u in the velocity correlation for the turbulent natural convection (see Eq. (22)), in such a way as to fit the temperature distribution found in the 3D simulation (Figs. 2-3 and 2-4). The sawtooth modulations of the ullage pressure induced by the He pulses were fitted to the telemetric data. For the fitting we chose parameters of He impulses in Eg. (21) (the pulse duration τ_{pulse} and its front and tail durations τ_{front} and τ_{tail}).

$$h_F^{tur} = 0.15\beta_h K_{L/G}\frac{(Ra_x\Psi)^{1/3}}{x} \propto \beta_h x^0, Ra_x = \frac{g\cos\varphi_t\beta_T C_{L,G}\rho_{L,g}(T_{LW}-T_L)x^3}{\mu_{L,G}K_{L,g}},$$

$$u_{N,x} = \beta_u \bar{u}_N(x), \bar{u}_N(x_i) = 0.178\frac{\nu}{x_i}\left(\frac{Ra_x \Pr}{1+0.494\Pr^{2/3}}\right)^{1/2} \propto \beta_u x^{1/2} or\ \bar{u}_N(x_i) = \left(\frac{g\beta_T q_{env}x}{C_{L,G}\rho_{L,g}}\right)^{1/3} \quad (22)$$

$$j_N = 2\pi R_{tank}\delta_x u_{N,x}\rho_{L/G} \propto \beta_u x^{31/30},$$

$$\delta_x = 0.565x\left[\left(1+0.494\Pr^{2/3}\right)/Ra_x\Pr^{23/15}\right] \propto x^{7/10}$$

The fitting gave the following values for the parameters:

- β_u= 0.05
- τ_{front} = 0.09sec, τ_{tail} = 0.5sec, and $\tau_{pulse} \approx 0.7$sec.
- The threshold pressure for a He pulse generation p_{th} is chosen to fit experimental data shown in Fig. 2-7.

Result of fitting the ullage pressure is shown in Fig. 2-7. We see that results of the MNM simulations fit very well the STS-115 data. We reemphasize that the only fitting parameter for the MNM, was the numerical coefficient β_u in the correlation relation for the natural convection velocity. This coefficient depends on properties of the fluids and is essentially independent of the tank design. Therefore we used MNM with this fitting parameter for analysis of the LOx SLS tank.

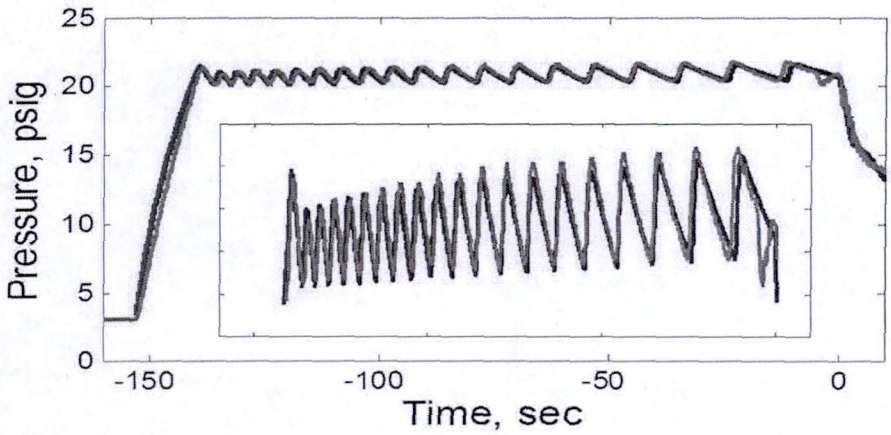

Fig.2-7: Ullage pressure during the pre-pressurization: STS115DB telemetry (red) and MNM simulation (blue). Results of the fitting with β_u=0.05, τ_{front} = 0.09sec, τ_{tail} = 0.5sec, and τ_{pulse} = 0.7sec.

Result of fitting of the MNM simulations of the ullage pressure teeth induced by the He pulses for other Space Shuttle flight is shown in Fig. 2-8. In order to fit the STS135 telemetry data He pulse parameters were changed only ~ 10% in comparison with the STS 115 values (Fig.2-7).

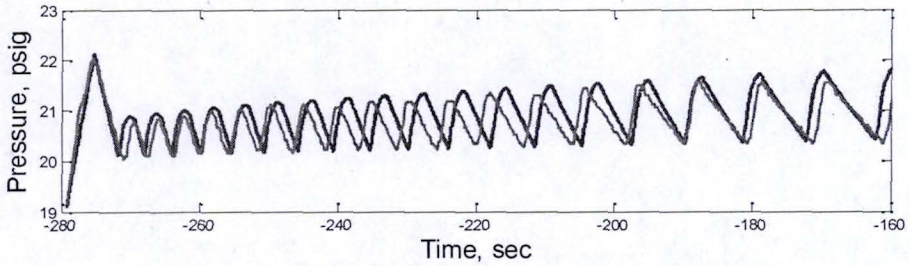

Fig.2-8: Ullage pressure during the pre-press (-280sec<t<-160sec): STS135DB telemetry (green) and MNM simulation (blue). Results of the fitting with β_u=0.05, τ_{front} = 0.09sec, τ_{tail} = 0.45sec, and τ_{pulse} = 0.75sec.

The fitting parameters of the MNM are further used in modeling the pre-pressurization and fight regimes to assess the risks for the proposed design of the SLS tanks (Section 5).

Numerical MNM and 3D simulations of the time-traces of the temperature of the ullage and wall at some regions of the tank are shown in Fig. 2-9 for β_u= 0.05 and rectangular He pulses of nominal amplitude j_{He}=0.3lb/sec=0.136kg/sec and duration 0.5sec. One can see that the corresponding curves for MNM and 3D simulations are closed enough (see also below Fig. 3-6). These results substantiate choose the value of β_u= 0.05.

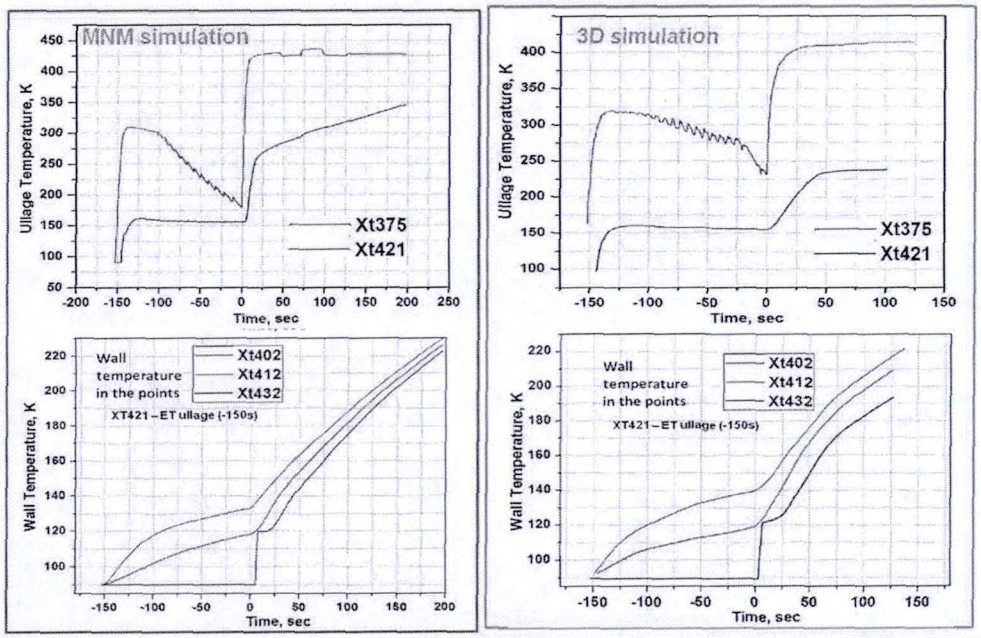

Fig.2-9: Time-traces of temperatures of ullage (upper line) and tank wall (lower line) in various layers in the tank: green curve corresponds to the layer near tank top. Results of the MNM simulation (left) and 3D simulation (right).

3 Operation during the fight

The GOx is used to cool the nozzles, where it is heated to the temperature T_{GOx}= 800R=444K. The hot gas is further injected into the LOx tank to keep the pressure at the required value which would otherwise decrease due to the LOx level lowering during the fight.

The rates of the LOx propellant and hot GOx flows controlling the ullage pressure are shown in Fig.3-1.

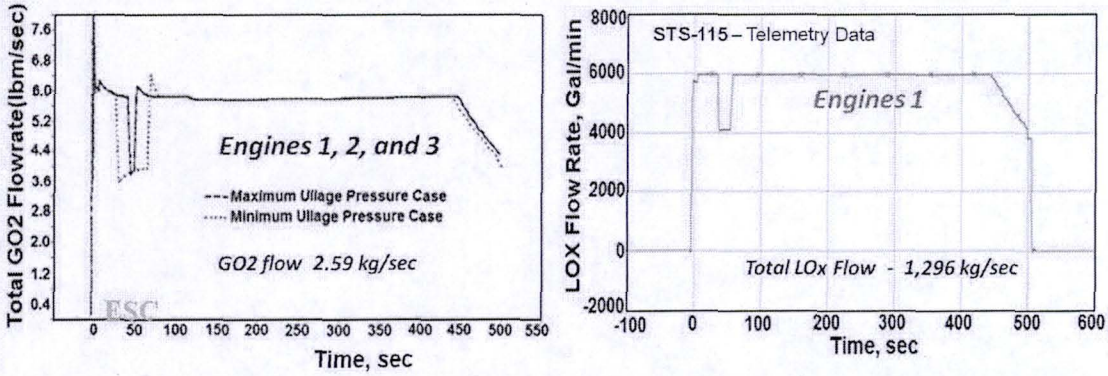

Fig.3-1: Flow rates of hot GOx into the tank and LOx from the tank during the flight.

To fit the STS-115 data [2] the form of dips seen on the curves in Fig. 3-1 was slightly modified for the MNM simulations (~ 10%). The rates correspond to the nominal values presented in Fig. 3-1. Result of fitting the ullage pressure and temperature are shown in Figs. 3-2 and 3-3, respectively. The ullage pressure falls within (20.5÷14.5) psig range and the temperature -- within (-100÷100)F=(200÷310)K range. We see that the results of MNM pressure simulations fit fairly well the STS-115 data (Fig.3-2).

The deviation of the simulated temperature from the data is substantial during the flight but small at the pre-pressurization stage (t<0, Fig.3-3). In the latter case, as can be seen in Fig. 3-4, the width of the transition region for the temperature is very small (< 2cm) and we conjecture that the temperature sensor is located outside this region. The observed deviation of the experimental and simulated temperature during the flight (Fig. 3-3) can be attributed to location of the detector in the relatively cold transition region which is larger during the flight, ~ 5cm (Fig. 3-4). Another possibility for the deviation is suggested by the 3D simulations (Fig. 3-5) which shows pocket of relatively cold gas in trapped in the upper corners of the ullage, where presumably the detector was located. These pockets are absent during the pre-pressurization (Fig. 2-3), which is a consequence of the relatively low density of He compared to GOx.

Time traces of the ullage and wall temperatures at various locations in the tank are shown in Fig. 3-6. They correspond well to the pronounced temperature stratification detected in the 3D simulation (Figs. 3-5 and 3-6). The 3D simulation also shows that the initial complex temperature distribution (Fig. 3-5, t=2sec) is transformed into almost flat layers after 10sec. This result justifies the approach adopted in the MNM.

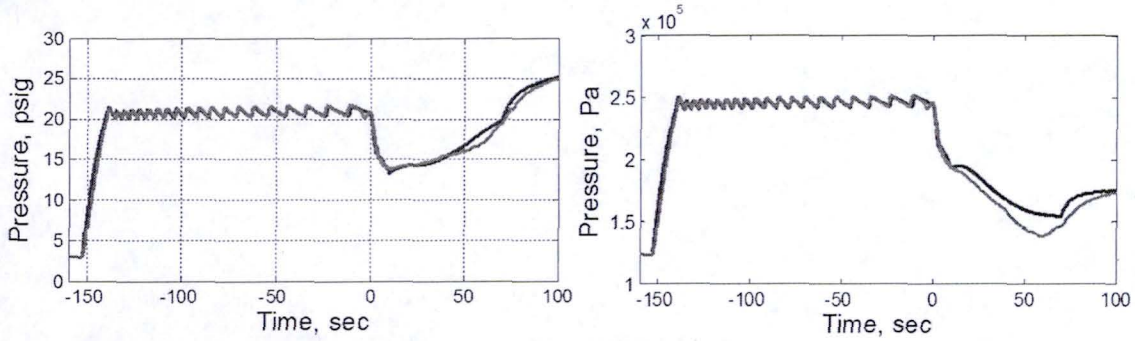

Fig. 3-2: Time-traces of ullage pressure during the pre-press and the initial stage of the flight in relative (left) and absolute units (right). STS115DB telemetry (red) and MNM simulation (blue).

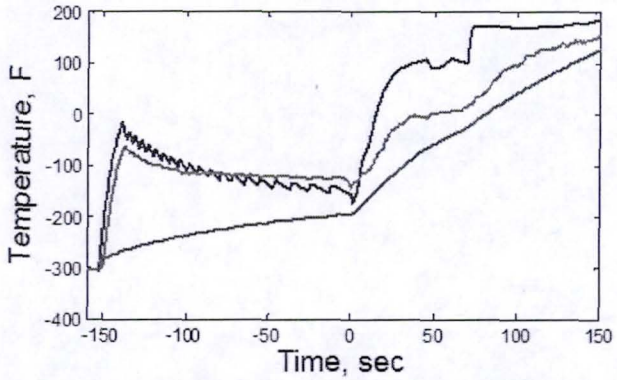

Fig. 3-3: Time-trace of ullage temperature during the pre-pressurization and the initial stage of the flight near the tank top where the thermo-sensor is located: STS115DB telemetry (red) and MNM simulation (blue). The green curve shows time-trace of the wall temperature.

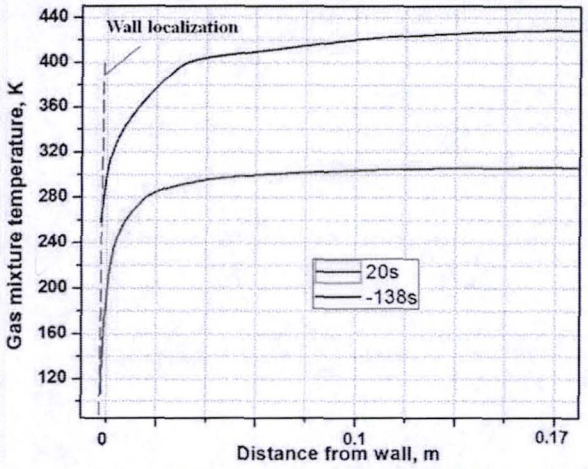

Fig. 3-4: Ullage temperature radial distribution at the level of the thermo-sensor location. Results of 3D simulation.

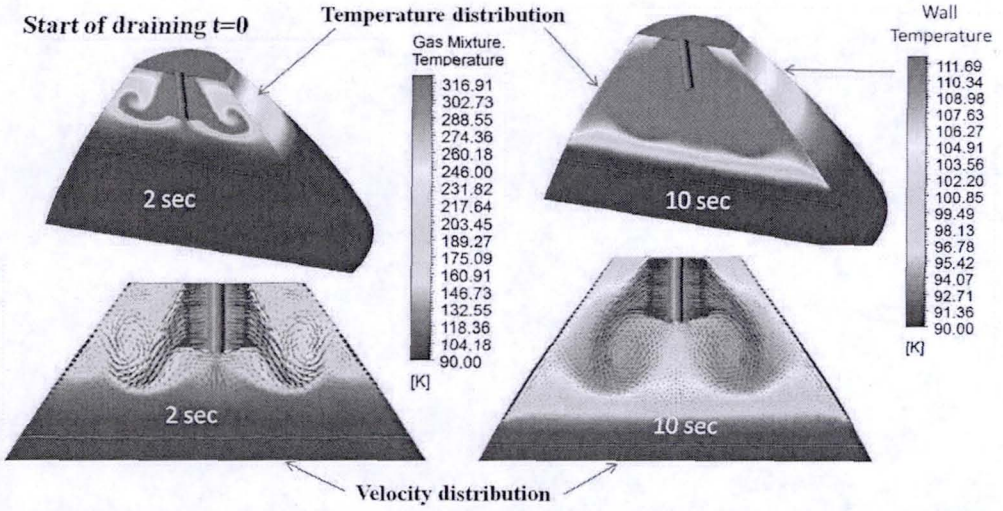

Fig.3-5: Temperature and velocity distributions at t = 2sec and t = 10sec after the start

Fig. 3-6 shows that the increase of the wall temperature lags behind the growth of the ullage temperature. The lag is $\tau_{gw} \approx 100\text{sec}$ which confirms theoretical predictions based on the estimates in Sec. 1.5. Time-traces of the partial pressures of GOx and He are shown in Fig. 3-7.

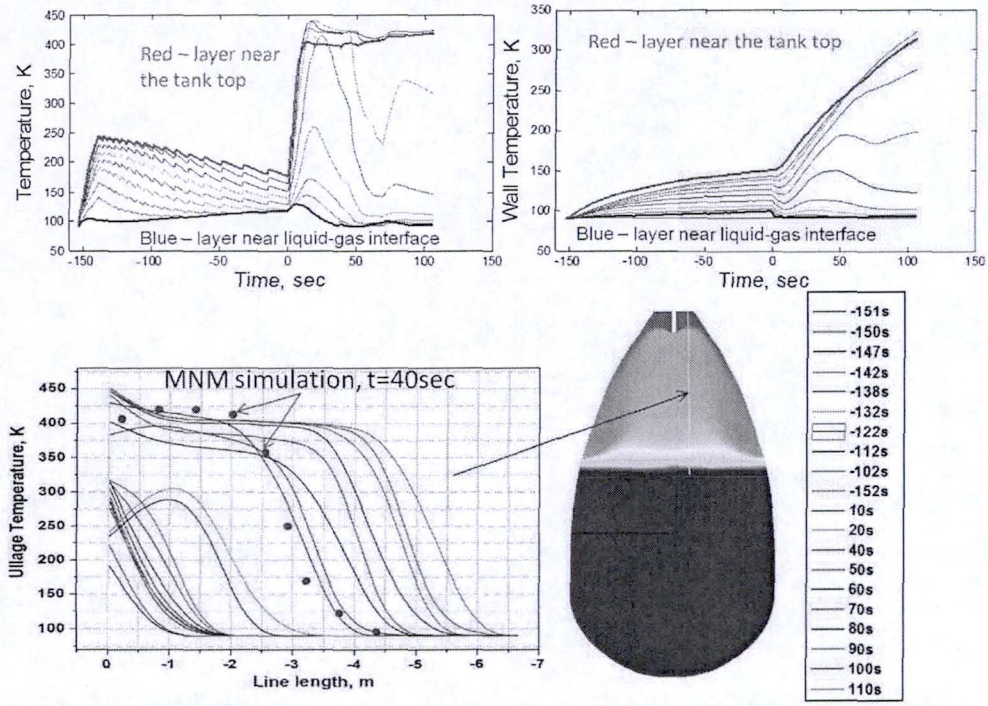

Fig.3-6: Time-trace of temperatures of gas ullage (left) and tank wall (right) in various layers in the tank: red and blue curves correspond to the layers near tank top and gas-liquid interface, respectively. Results of the MNM simulation.

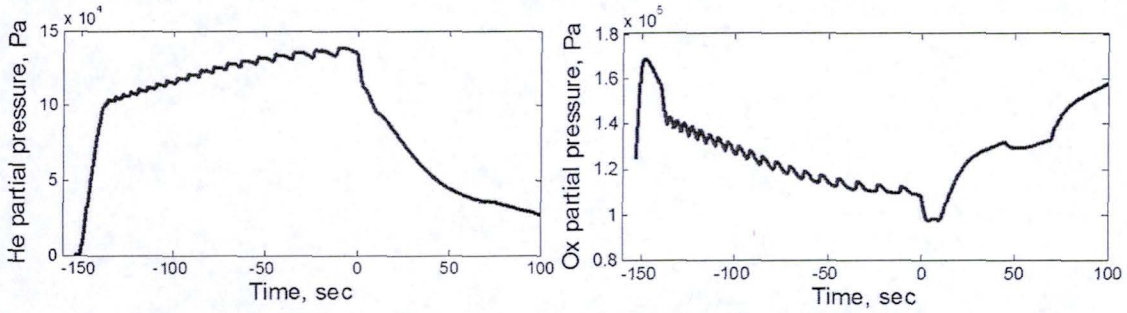

Fig.3-7. Time-traces of partial pressure of gaseous Ox and He in ullage layer near the liquid-gas interface. Results of the MNM simulation.

Dynamics of the condensation rate and the condensed mass are shown in Fig. 3-8. Evaporation is seen to override condensation during the first stage of the flight (0<t<10sec, Fig.3-8). This result is explained by the stratification of partial pressure of Ox and He gases and the dynamics of the ullage pressure. Indeed, the ullage pressure drops sharply during of the first stage of the flight (Fig. 3-2) following a rapid decrease of the liquid's level. The partial GOx pressure drops and approaches 1atm (Fig. 3-7, left). As a consequence, the interface temperature T_s decreases to the value T_L (see Eq. (3)) and the condition Eq.(9) breaks down, implying that evaporation becomes dominant. Later on, the partial GOx pressure increases (Fig. 3-7, left) due to the GOx pumping. As a result, evaporation becomes overridden by

condensation (Fig. 3-8). Total mass of the condensed $M_{cond} \leq 1$kg (Fig. 3-8, right), i.e., it is negligible compared to the total mass injected hot GOx: M_{GOx}=1.3kg/sec $\times$ 100sec=130kg. *This means that in contrast to the pre-pressurization stage the contribution of condensation-evaporation process to the overall mass and heat balance during the flight (t>0) is very small.*

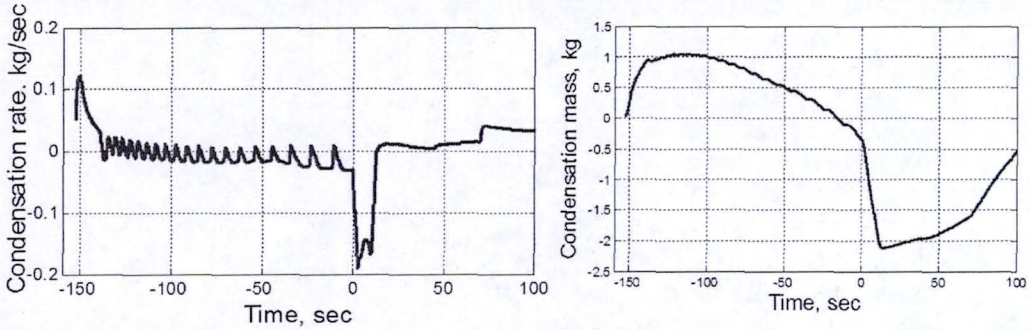

Fig.3-8. GOx condensation rate (left) and total condensed mass (right). Results of the MNM simulation.

4 The limiting case of fully mixed gases

The pronounced stratification of both ullage temperature and partial pressure of GOx and He was found in the 3D simulation (Fig. 3-5). The stratification is also observed in the MNM simulation provided one uses the value $\beta_u = 0.2$ in the correlation for the velocity given by Eq. (22). This value of β_u is chosen in the MNM simulation to best fit the average velocities given by the 3D simulation. It should be noted that the value of β_u for small variations of the gas density where the correlations Eq. (22) strictly hold is $\beta_u \approx 1$. For large temperature gradients near the wall the variations of the gas density may be substantial. Therefore, it is instructive to consider the ullage gas dynamics for $\beta_u = 1$, where due to higher velocity of natural convection near the wall, the temperature stratification almost totally vanishes (Fig. 4-1) and stratification of partial GOx and He pressure is very weak (Fig.4-2).

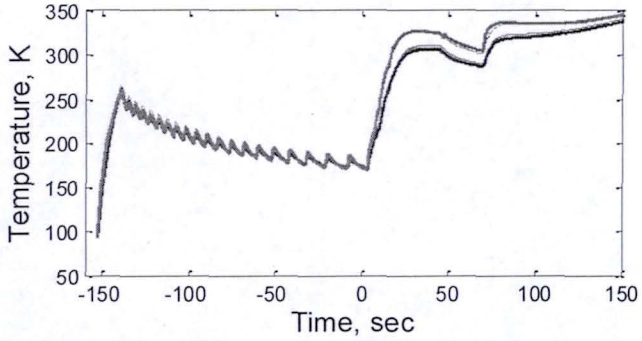

Fig.4-1: Ullage temperature time-trace at various locations in the tank: red and blue curves correspond to the layers near tank top and interface, respectively. Results of the MNM simulation for $\beta_u = 1$.

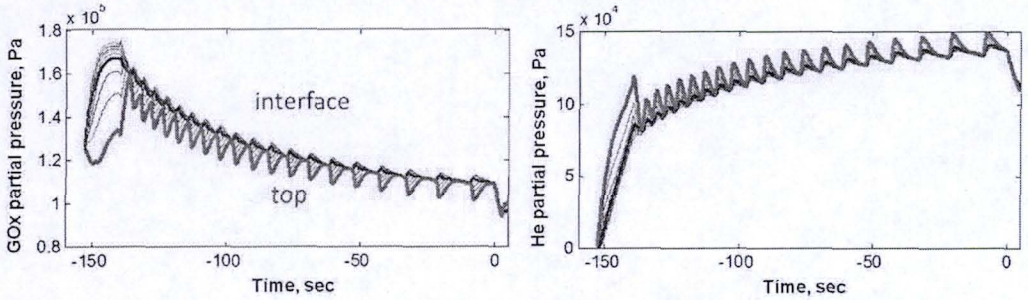

Fig. 4-2: Time-traces of partial pressure of GOx and He in the ullage; red and blue *curves correspond to layers near the top and the bottom of the tank, respectively.* Results of the MNM simulation for $\beta_u = 1$.

However, even in this limiting case of total mixing of the two gases, the time traces of the ullage pressure and temperature do not change considerably (see Fig.4-3 ÷Fig. 4-5).

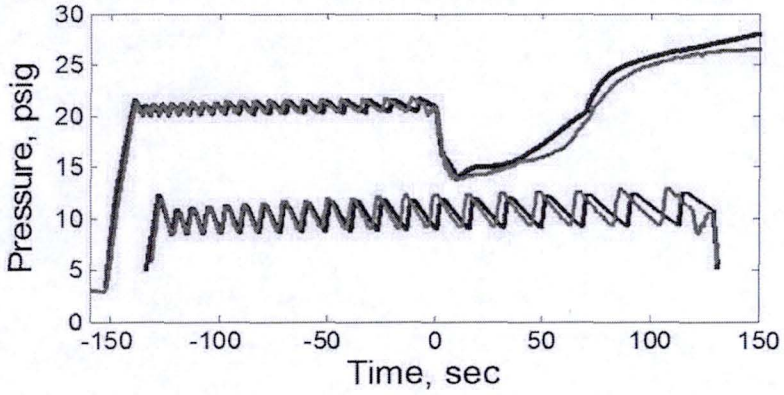

Fig. 4-3: Time-traces of ullage pressure. STS115DB telemetry (red) and MNM simulation (blue). Results of the MNM simulation for $\beta_u = 1$.

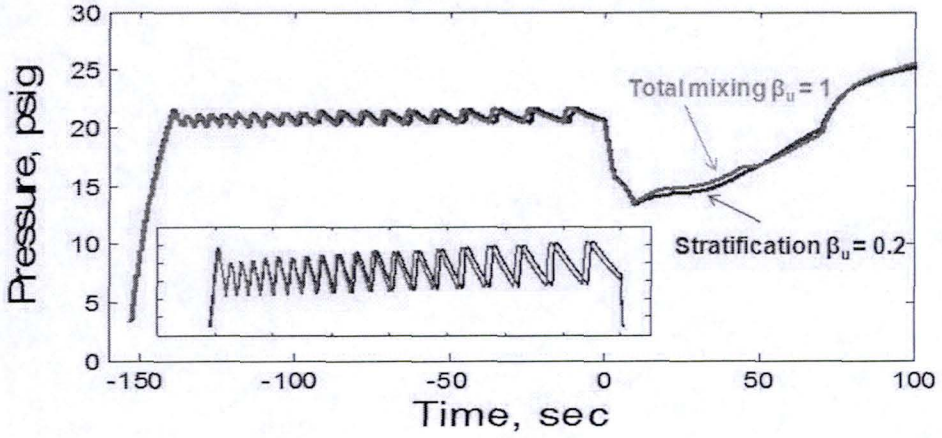

Fig. 4-4: Time-traces of ullage pressure; blue for stratification ($\beta_u = 0.2$) and green for total mixing case ($\beta_u = 1$). Results of the MNM simulation.

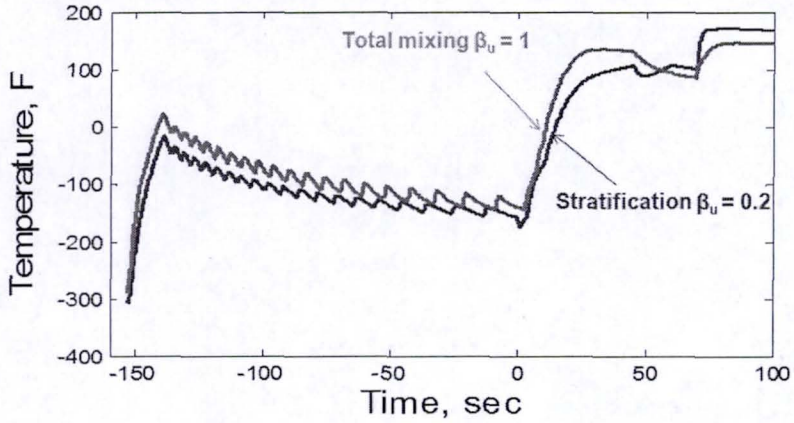

Fig. 4-5: Time-trace of ullage temperature near the tank top: blue for stratification (β_u= *0.2*) and green for total mixing case (β_u= *1*). Results of the MNM simulation.

In the case of total mixing the average condensation rate and, accordingly, the total condensed mass are smaller than those for stratification (Fig. 3-7, β_u= *0.2*) during the late pre-pressurization stage (Fig. 4-6, t<0). On the other hand, they are essentially identical during the early pre-pressurization stage and the flight (Fig. 4-6, t>0). The decrease of the condensation in the absence of stratification during the pre-pressurization stage is explained by the increase of the gas temperature and decrease of the partial pressure of GOx near the interface compared to dynamics with stratification. The partial pressure decrease leads to decrease of the surface temperature T_s in the right-hand-side of inequality(9), while the rise of the gas temperature T_g makes the left-hand side of the inequality larger. Both lead to inhibition of condensation and acceleration of evaporation, which explains the observed dynamics (Fig. 4-6).

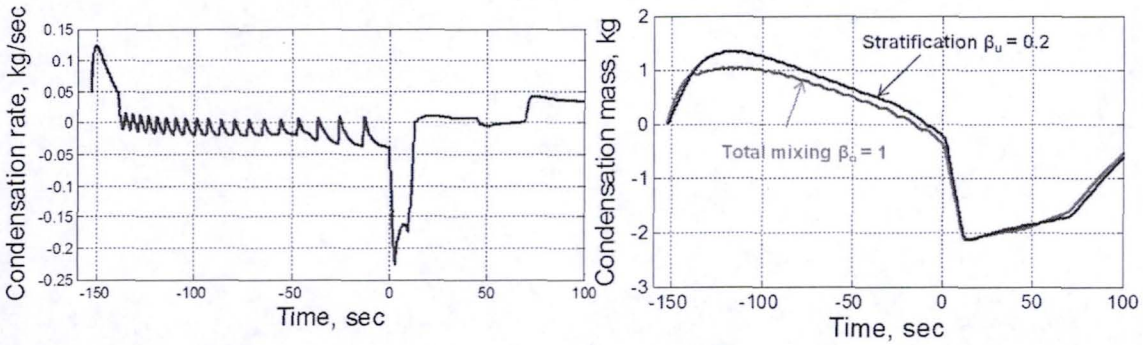

Fig.4-6. GOx condensation rate (left) and condensed mass (right). Results of the MNM simulation for β_u= *1*.

5 Scaling of the risks

5.1. Scaling of pressure near the feedline top and bottom

The pressure in LOx tank feedline is high due to hydraulic pressure of a large mass of LOx. The total pressure near feedline top p_{top} and bottom p_{bot} are

$$p_{bottom} = g\rho_L\left(H_{\text{tank}} - L_{ullage} + L_{pipe}\right) + p_{ullage} = 5.9\ atm\ \ (t < -150s, p_{ullage} = p_{atm})$$
$$p_{top} = g\rho_L\left(H_{\text{tank}} - L_{ullage}\right) + p_{ullage} = 2.56\ atm\ (5.45 atm \text{ at max acceleration}), \quad (23)$$

The pressures during pre-pressurization for 3 and 5 engines are approximately equal to

$$p_{top} \approx \begin{cases} 2.6(3.6)\,atm\ at\ t < -152\text{s},\ \text{p}_{\text{ullage}} \approx 1\text{atm} \\ 4(5)\,atm\ at\ -138\text{s} < \text{t} < 0,\ \text{p}_{\text{ullage}} \approx 2.45\text{atm} \end{cases},$$
$$p_{bottom} \approx \begin{cases} 5.9(9.2)\,atm\left(t < -152\text{s},\ \text{p}_{\text{ullage}} \approx 1\text{atm}\right) \\ 7.3(10.6)\,atm\left(-138\text{s} < \text{t} < 0,\ \text{p}_{\text{ullage}} \approx 2.45\text{atm}\right) \end{cases} \quad (24)$$

The Shuttle achieves maximal acceleration $g_{rocket}=2.5g_0$ at the point t=80sec, when the liquid level is 1.69m above the tank bottom (Fig.5-1). The maximal top and bottom pressures corresponding to total acceleration $g = 3.5g_0$ are approximately equal

$$p_{top} = 5.8(8.5)\,atm\ at\ \text{t}>50\,\text{sec},\ \text{p}_{\text{ullage}} \approx 1.75\text{atm},$$
$$p_{bottom} = 17.5(28)\,atm\left(\text{t}>50\,\text{sec},\ \text{p}_{\text{ullage}} \approx 1.75 atm\right) \quad (25)$$

For estimation of the hydrostatic pressure in the feedline for the SLS tank with 5 engines we assume that the tank height and pipe length scale as $5/3H_{tank}$ and $5/3L_{pipe}$ (H_{tank} =15.05m and L_{pipe} =29.4m are the parameters of Shuttle LOx tank).

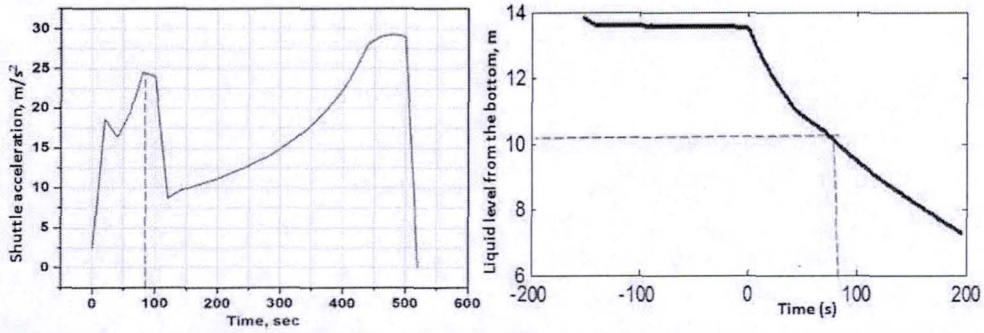

Fig.5-1 Time traces of Shuttle acceleration (left) and the liquid level in the tank (right).

Thus, the maximal pressure at the bottom of the feedline for SLS with 5 engines will reach 28atm. Such high pressure in the pipe and the engine's inlet has to be taken into account for the development of SLS.

5.2. Scaling of shape and size of the LOx tank for SLS with 5 engines

Two possible shapes of the SLS tanks are considered in this work: (i) the Shuttle LOx-tank shape and (ii) the Shuttle LH2-tank shape with volume upscaled to 5/3 of the Shuttle LOx tank (Fig. 5-2). The diffuser size is changed in the case (ii) (Fig.5-2) to prevent contact with the liquid surface. The initial ullage volume V_0 and the volume in end of pre-pressurization V_1, i.e., at the points t=-152sec and t=-138 sec (see Fig. 2-1), respectively, are increased by the factor 5/3: V_0=8.43m^3 and V_1=13.2m^3. The fluxes of hot He and GOx are also increased by the factor of

5/3 compared to the Shuttle. Fig. 5-2 also shows the gas velocity field near the diffusers for both shapes of LOx SLS tanks.

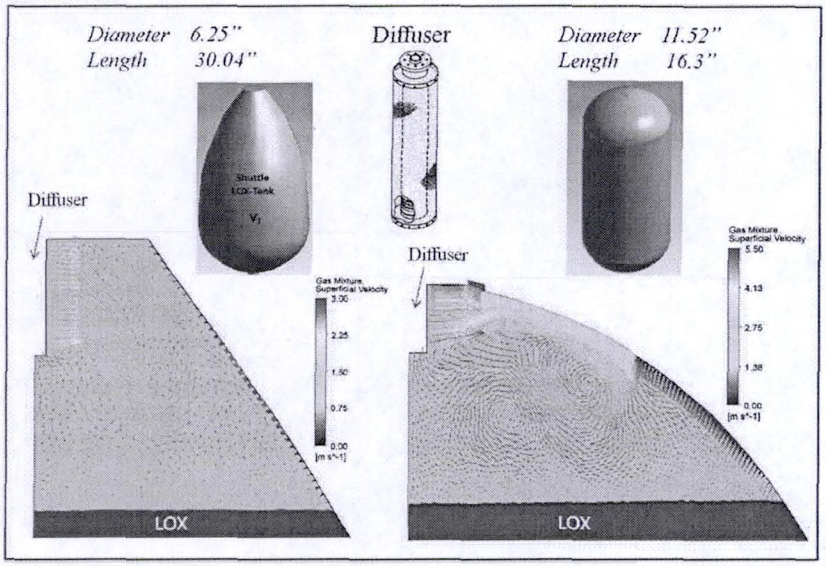

Fig.5-2 The shapes of SLS tanks and diffuser considered in this work: (i) the Shuttle-LOx-tank shape (left); (ii) the Shuttle-LH2-tank shape (right).

Predicted time-traces of the ullage pressure and temperature for the two shapes of SLS tanks are shown in Fig. 5-3 and compared to the Shuttle nominal time-traces.

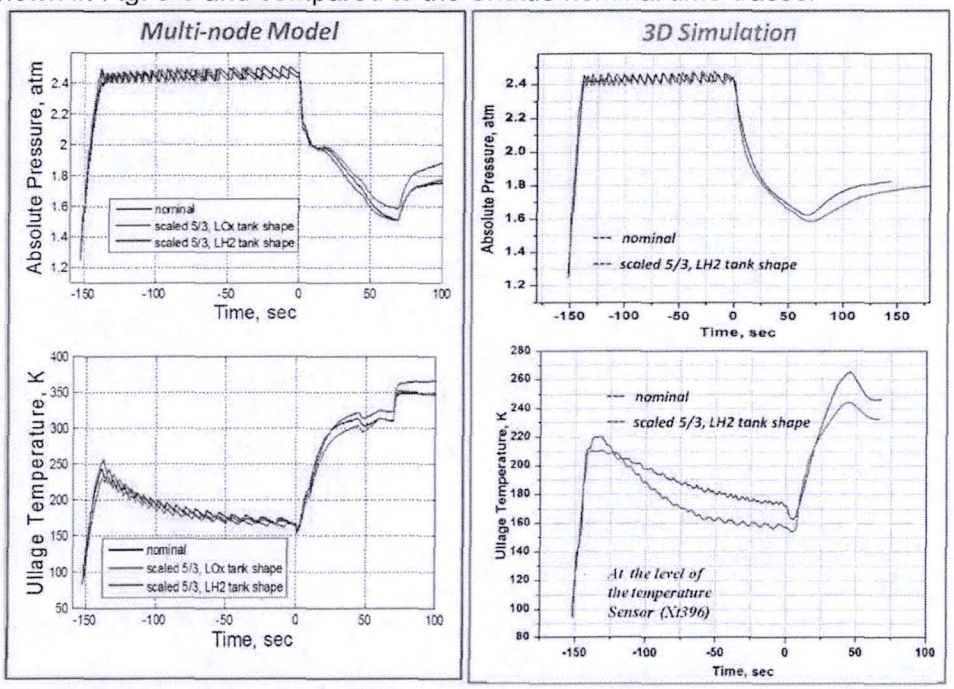

Fig.5-3 Predicted time traces of ullage pressure and temperature for different shapes of the SLS LOx tanks. Results of MNM and 3D simulations.

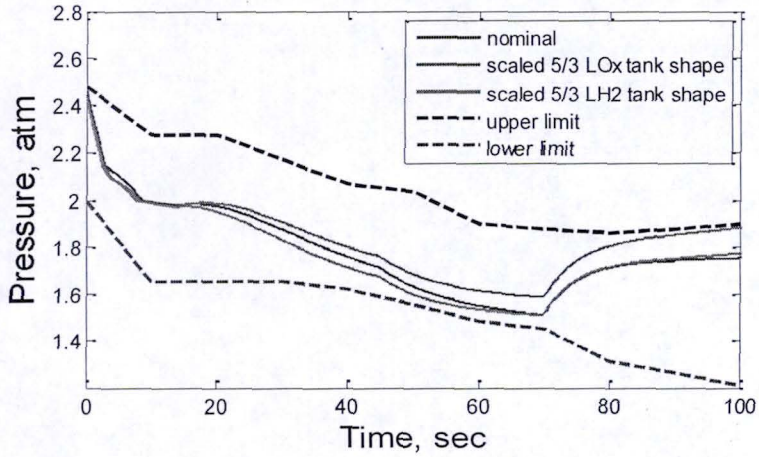

Fig.5-4 Predicted time traces of ullage pressure for different shapes of the SLS LOx tanks. Results of the MNM simulation.

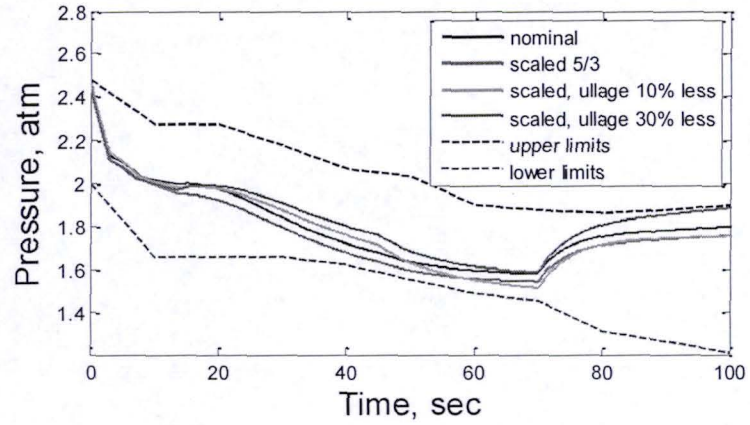

Fig.5-5 Predicted time traces of ullage pressure for LH2 shape of the SLS LOx tanks with different initial ullage volumes. Results of the MNM simulations.

One can see that the time-traces of ullage pressure for the two LOx tank designs are close to one another. It is important to note that the predicted pressure time-traces lie within the band of acceptable ullage pressure (Fig. 5-4). However, the pressure time-trace for the LOx tank of shape (ii) lies very close to lower bound of the band, creating hazardous situation. To analyze the possibilities of controlling the risks we carried out the simulation for several other initial ullage volumes and showed that the situation can be substantially improved if the initial ullage volume in the LOx tank is decreased by 10% (Fig.5-5).

6 Effect of sloshing in the LOX tank

Intensive sloshing of cryogenic liquid (LOx) can occur after the start due to vibration of the rocket. Sloshing of cryogenic liquids can change the ullage pressure due to variations of the heat and mass fluxes at the liquid-vapor interface and near the tank wall. Two main types of sloshing are shown in Fig. 6-1. Generally, the motion of the LOX tank during the lift-off can be decomposed into three major components: twang, breathing, and oscillation. The twang occurs

before the lift-off, while the breathing and the oscillation occur during the lift-off. The twang occurs approximately 5 seconds before the lift-off when the main engines are ignited and the Shuttle is released from the launch pad. When the main engines are ignited, a torque is created around the attachment point of the rocket boosters which makes the entire vehicle tilt [9]. The tip of the ET tilts as far as 30 inches from the rest position and then returns back. When the tank returns to the near vertical position the solid rocket boosters are ignited and the launch takes place.

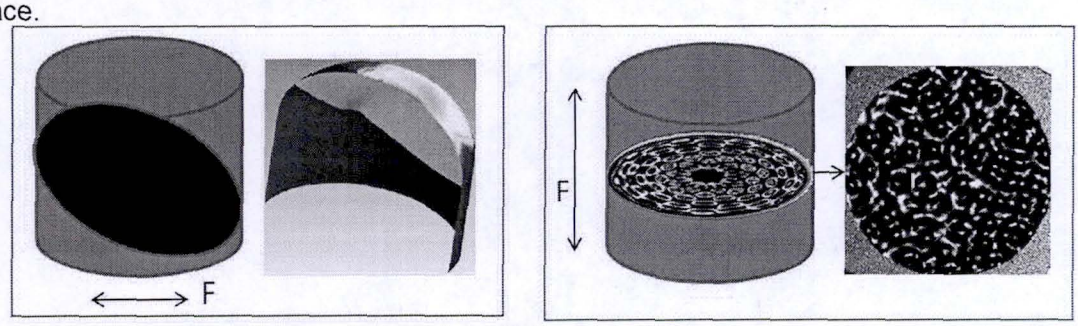

Fig.6-1 Two main types of sloshing: (i) Longitudinal sloshing waves excited by lateral forces (left); (ii) Axial sloshing (capillary waves) excited parametrically by axial vibrations (right)

This motion initiates oscillations of the liquid surface with period T_{osc}~*2.5 sec* and amplitude a_{osc}<*0.5m* (Fig. 6-2).

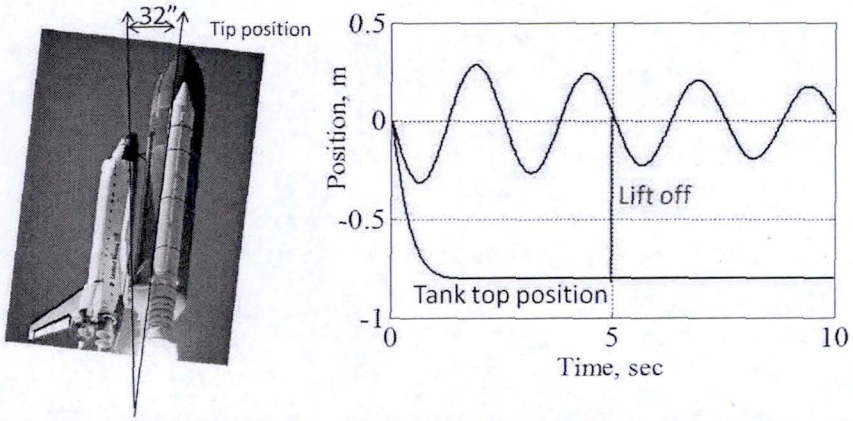

Fig.6-2 Tilting of the Shuttle from the vertical direction after the lift-off (left) and typical sloshing oscillations (right).

6.1. Longitudinal sloshing waves

The rocket oscillation leads to variation of the liquid level near the tank wall [12,13]. Our 3D simulations showed that the wall temperature near the liquid-vapor interface is lower than the boiling temperature (T_{boil}>100K at p>2.25atm) for distance from the interface less than 0.75m during both pre-pressurization and the flight (see Fig. 6-3). It means that the variation of the liquid level near the tank wall will not stimulate evaporation of the liquid provided the oscillation amplitude a_{osc} is smaller than 0.75m. This condition is apparently satisfied even for the Shuttle (see Fig. 6-2).

The SLS design differs from the Space Shuttle construction in that no torque on the rocket is created by the engines ignition. As a consequence the hazard associated with the twang of the ET is essentially eliminated in the SLS design.

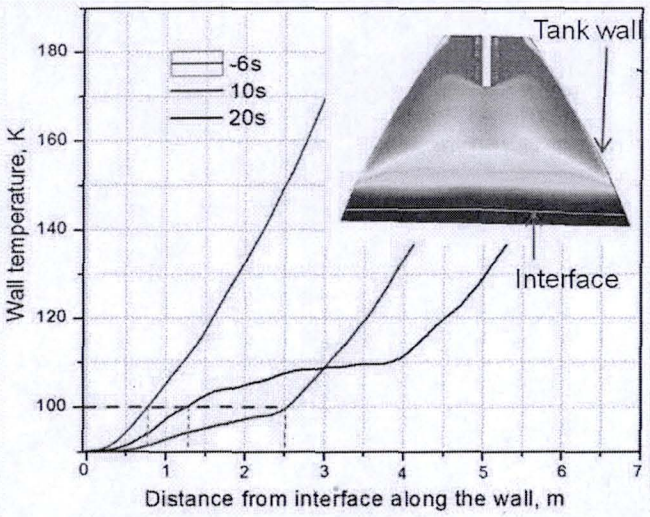

Fig.6-3 Distribution of the wall temperature near the liquid-vapor interface for different times (x=0 is the interface position for a given time). Results of 3D simulation.

After the start (t > 0) the stationary longitudinal sloshing oscillating waves enhance condensation due to (ii) increasing the area of the liquid surface and (mainly) due to (ii) mixing the heated surface liquid layer with adjacent cold LOx with $T=T_L$. As a result of mixing the heated surface layer became narrower but the interface temperature did not change, it is given by the partial GOx pressure: $T = T_s(p_{GOx}) \approx 100K$. The condensation flow rate at the liquid-gas *interface is limited by heat balance between the hot gas* T_g *near the surface and the liquid* surface with $T=T_s$:

$$j_{cond}(t) = \left[K_L \frac{T_s - T_L}{L_L(t)} - K_g \frac{T_g - T_s}{L_g(t)} \right] \frac{1}{q_L + C_g \left(T_g - T_s \right)}. \qquad (26)$$

The maximum value of the condensed mass M_{cond} induced by the intensive sloshing can be estimated assuming complete mixing of the surface layers of cold and warm liquid over each period of oscillation. Due to such intensive mixing the width of the heated liquid layer over a fraction S_L^* of the surface area will be very small at end of each oscillation, $L_L \to 0$ (Fig. 6-4).

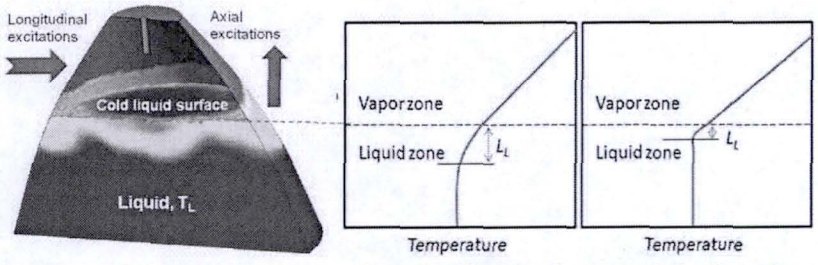

Fig. 6-4. Sketch of the temperature distribution before and during the sloshing

In this case the first term in the right part of Eq. (26) is much larger than the second. Therefore, the mass condensed for one period can be estimated as

$$M_{cond}(T_{osc}) = \int_{o}^{T_{osc}} S_L^* J_{cond}(t_1) dt_1 \approx S_L^* (T_s - T_L) \frac{\sqrt{K_L C_L \rho_L T_{osc}}}{q_L + C_{H2}(T_g - T_s)} \left(\sqrt{\frac{4}{\pi}} \right), \quad (27)$$

The total condensed mass induced by the longitudinal waves over the time of t is given by

$$M_{cond}^{slosh}(t) = M_{cond}(T_{osc}) \frac{\Delta S_L + S_L}{S_L} \left(\frac{t}{T_{osc}} \right), \quad (28)$$

The total condensation flux is equal to

$$\max J_{cond}^{slosh} = \frac{\max M_{cond}^{slosh}(t)}{t} = 0.26 \frac{kg}{\sec} \quad (29)$$

$$\text{for} S_L^* \approx S_L / 3, T_s(p_{GH2}) = 100K, 100K < T_g \le 200K \text{ near the interface}$$

It should be compared to the much larger the flux of the injected hot GOx: $J_{GOx} = 2.6 \frac{kg}{\sec} \times [N_{nozzle} / 3]$, N_{nozzle} – number of nozzles in SLS

Thus, the longitudinal sloshing waves cannot appreciably change the ullage pressure.

Effect of sloshing is expected to be even smaller for the SLS since the flow rate of injected hot GOx will increase with larger nozzle number. However, SLS vehicle has higher thrust and one can expect stronger vibrations due to adding one or two RS-25 engines.

6.2. Axially excited sloshing: generation of droplets

The thrust oscillations initiate axial excitation and lead to Faraday instability of the liquid surface. Intensive oscillations of these modes can result in the liquid level discontinuity and generation of the liquid droplets under the liquid-gas interface. This process will change heat balance on the interface. Evaporation of the cold liquid droplets into the hot ullage gas can increase the ullage pressure during the beginning stage of the flight. At the same time enlarging the cold surface can accelerate condensation. Since the rate of evaporation of liquid Oxygen depends on partial pressure of gaseous Ox, in the case where He is used as the pressurization gas we expect enhanced evaporation and consecutive increase in a ullage gas pressure. For gaseous oxygen pressurization these droplets will enhance the condensation rate.

Dispersion relation for small wavelength capillary wave can be presented as [12,13]:

$$\omega^2 = \left(gk + \frac{\sigma}{\rho} k^3 \right) \tanh(kh)$$

where σ is surface tension, k=2π/λ, λ as the wavelength, k is the wave number and ρ is the liquid density. At small k<<1

$$\omega_{mn}^2 = \frac{g\lambda_{mn}}{a} \tanh(\lambda_{mn} h / a) \quad (30)$$

The nonlinear dynamics of the droplet formation and ejection is very completed and strongly depends on the rocket vibrations spectrum. Here we carry out a simplified analysis this dangerous effect. The typical diameter of ejected droplets is about [14,15]

$$d_{drop} \simeq (\sigma_L / \rho_L)^{1/3} \omega^{-2/3}, \quad \omega = 2\pi f \quad (31)$$

where ρ_L=*1141kg/m*^{3} and σ_L=*0.0135N/m* are liquid density and surface tension, ω is vibration frequency ($\omega=2\pi f_{vibr}$). Characteristic values of d_{drop} are shown in Fig.6-5 (left): $d_{drop}(25Hz) \simeq 0.8mm$ and $d_{drop}(200Hz) \simeq 0.2mm$.

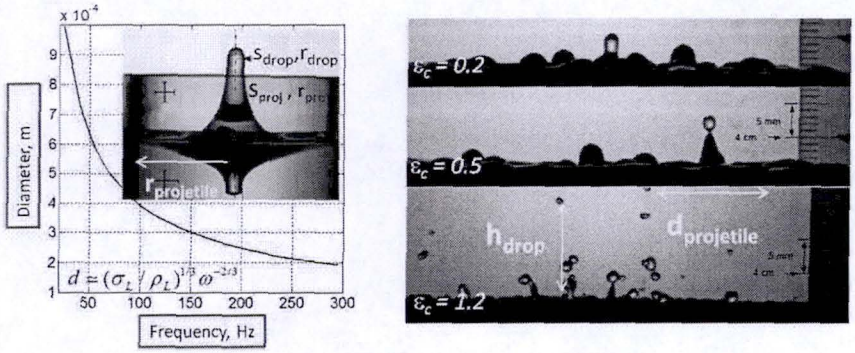

Fig.6-5. Typical diameter of ejected droplets depending on thrust oscillation frequency (left) and generation of droplets under action of supercritical vibration acceleration $\varepsilon_d>0$ [13].

Each projectile area of diameter $d_{proj} \approx 5d_{drop}$ ejects the droplet with a rate given by [14,15]

$$dn/dt \equiv \dot{n} = 0.04\varepsilon_d^{2.8}\omega\,[s^{-1}], \varepsilon_d = (a_{vibr} - a_d)/a_d,$$
$$a_d = 0.26(\sigma/\rho)^{1/3}\omega^{4/3} \tag{32}$$

Here a, ω are vibration acceleration and frequency, a_d is the critical driving acceleration for the onset of droplet ejection. The droplet ejection occurs if vibration acceleration $a_{vibr} > ad$, i.e. when the frequency and amplitude vibration A_{vibr} satisfy the condition:

$$a_{vibr} = A_{vibr}\omega^2 > a_d \text{ or } A_{vibr} > A_c = 0.1mm(65Hz/f_{vibr})^{2/3},$$
$$A_c = 0.2mm \text{ for } f = 25Hz, A_c = 50\mu m \text{ for } f = 200Hz \tag{33}$$

Sufficiently strong vibrations can occur only after the start. At this point the thermo-diffusion length in the liquid has increased to the value of L_D (100sec)≈7mm during the prepress (t ≈ 100sec). This value is much greater than the typical drop diameters: $L_D \approx 5mm >> d_{drop} \text{ for } f > 50Hz)$. It follows that inner temperature of generated droplets T_{drop} is close to the surface temperature of the liquid $T_s(p_{GOx})$. Therefore, the liquid mass evaporated due to the vibration is very small. Indeed, the mass evaporated with surface of single droplet s_{drop} during the droplet life-time t_{drlife} can be estimated as

$$m_{evap}(t_{drlife}) = s_{drop}\int_{t_{press}}^{t_{press}+t_{drlife}} j_{evap}(t)dt \le \frac{J_{cond}(t_{press})s_{drop}}{S_L}t_{drlife}, t_{drlife} = \sqrt{\frac{2h_{drop}}{g}},$$
$$J_{evap}(t) = S_L\frac{\left(T_g - T_s(p_{GH2})\right)\sqrt{K_gC_g\rho_g} - \left(T_s(p_{GH2}) - T_{drop}\right)\sqrt{K_LC_L\rho_L}}{\left(q_L + C_g\left(T_g - T_L\right)\right)\sqrt{\pi t}}, \tag{34}$$

where h_{drop} is the maximum height an ejected droplet rises above the surface (see Fig. 6-5). The total evaporated mass is given by

$$M_{evap} \le m_{evaop}(t_{drlife})\frac{dN_{drop}^{total}}{dt}t = m_{cond}(t_{drop})\frac{S_L\dot{n}_{drop}}{s_{proj}}t,$$
$$where \frac{dN_{drop}^{total}}{dt} = \frac{S_L\dot{n}_{drop}}{s_{proj}}, \dot{n}_{drop} - \frac{dn_{drop}}{dt} \tag{35}$$

Here dN_{drop}^{total}/dt is total number of droplets ejected over unit time from the liquid surface S_L. Taking into account Eq. (34) and condition $d_{proj} \approx 5d_{drop}, s_{drop}/s_{proj} = 4/25$ we conclude from Eq.(35) that the total evaporation mass is a negligible quantity

$$M_{evap} \le J_{evap}(t_{press})t_{drlife}\frac{4\dot{n}_{drop}t}{25} \le \frac{4J_{evap}(T_{prepress})t}{25}, \dot{n}_{drop} \le \frac{1}{T_{drlife}}, \qquad (36)$$

$$J_{evap} \le M_{evap}/t = 0.16J_{evap}(T_{prepress}) \le 0.03g/\sec$$

In the estimation we used the results of calculation presented in Sec.2 (see Fig. 2-8) $J_{evap}(T_{prepress}) \le 0.2g/\sec$.

6.3. Combined action of longitudinal and axial sloshing vibrations

An appreciable effect can occur only as a result of combined action of intensive longitudinal and axial sloshing vibrations (Fig. 6-4, left)). The maximum value of the condensed mass induced by sloshing waves can be estimated assuming intensive mixing of surface layers of cold and warm liquid during each period. Due to such mixing the thickness of some area of the heated surface layer S_L^* will very small at end of each oscillation, $L_L \to 0$ (Fig. 6-4). Droplets generated by the axial sloshing will have T near $T_{L,}$, except for a very thin surface layer $L_L \to 0$ near the surface having $T=T_s(p_{GOX})$. In this case the maximum value of the condensed mass m_{cond} on the surface s_{drop} of a single droplet during the droplet life t_{drlife} can be estimated as

$$m_{cond}(t_{drlife}) = s_{drop}\frac{M_{cond}(t_{drlife})}{S_L} = \frac{s_{drop}\left(T_s(p_{GH2}) - T_L\right)\sqrt{K_L C_L \rho_L}}{q_L + C_{H2}\left(T_g - T_s\right)}\sqrt{\frac{4t_{drlife}}{\pi}}, \; t_{drlife} \approx \sqrt{\frac{2h_{drop}}{g}} \qquad (37)$$

The total mass flow rate of condensed vapor on all ejected droplets is

$$J_{cond}^{total} = m(t_{drlife})\frac{dN_{drop}^{total}}{dt} = \left(\frac{4}{25}\right)\frac{S_L^* m(t_{drlife})\dot{n}_{drop}}{s_{drop}}, \; \dot{n}_{drop} \le \frac{1}{t_{drlife}} \text{ for } A_{vibr} > Ac,$$

$$J_{cond}^{total} \le \frac{8S_L^*\left(T_s(p_{vapor}) - T_L\right)\sqrt{K_L C_L \rho_L}}{25\left[q_L + C_{vapor,p}\left(T_g - T_s\right)\right]}\sqrt{\frac{1}{\pi t_{drlife}}} \propto h_{drop}^{1/4}, \quad t_{drlife} = \sqrt{\frac{2h_{drop}}{g}}, \qquad (38)$$

Using $S_L^* \approx S_L/3$ and $t_{drlife} \approx \sqrt{2h_{drop}/g} \approx 0.02\sec$ we obtain from Eq.(38) that the total mass flow rate of condensed vapor on all ejected droplets is $J_{drop}^{total} < 0.45kg/\sec$. We notice that the rate of injected hot GOx mass flow is much higher: $J_{GOx} = 2.6(N_{nozzle}/3)\frac{kg}{\sec}$, N_{nozzle} – number of nozzles in SLS.

As a result of the condensation the ejected droplets will be heated and falling back into the liquid will increase the temperature of the liquid surface layer. The width of the heated surface liquid layer can be found from the heat balance equation

$$J_{drop}^{total}\left[q_L + C_{GOx}\left(T_g - T_s\right)\right]\cdot t = C_L\rho_L\left(T_s - T_L\right)S_L \cdot l_{heated}^{liquid},$$

$$l_{heated}^{liquid}(t) = \frac{S_L^*}{S_L}\left(\frac{8L_D(t)}{25\pi}\right)\left(t \cdot t_{drlife}\right)^{1/2}\dot{n}_{drop}, t_{drlife} = \sqrt{\frac{2h_{drop}}{g}}, \qquad (39)$$

$$l_{heated}^{liquid}(t_{flight}) \le 5L_D(t_{flight}) = 5cm \text{ for } \dot{n}_{drop} \le \frac{1}{t_{drlife}}, \; t_{drlife} \approx 0.02\sec$$

Thus, *combined action of longitudinal and axial sloshing vibrations can lead to formation of relatively thick hazard surface layer of heated liquid with temperature T≈23.8K, thickness L≈5cm, volume,* $V_{heat} = S_{tank} L_{heated}^{total} / 2 \approx 1.4 m^3$ *and mass* $M_{heat} = V_{heat} \rho_L \approx 1600 kg$. Total mass of LOx in the tank is 627500kg.

SLS vehicle has higher thrust and expected vibrations due to adding one or two RS-25 engines. At the same time all the effects under consideration are taking place in a small layer adjacent to the interface and the mass flow rate of injected hot GOx increases with the engine number. Therefore the influence of these effects on both the mass and the heat balance in the tank will not be critical. However, the effect of heating of relatively thin layer to T≈100.8K can arise in LOx SLS tank.

SLS vehicle has higher thrust and expected vibrations due to adding one or two RS-25 engines. At the same time all the effects under consideration are taking place in a small layer adjacent to the interface and the mass flow rate of injected hot GOx increases with the engine number. Therefore the influence of these effects on both the mass and the heat balance in the tank will not be critical. However, the effect of heating of relatively thin layer to T≈100.8K can arise in LOx SLS tank.

Conclusion

We performed theoretical investigation of main physics processes in LOX tank during pre-starting prepress and rocket flight that can lead to possible hazards in the case of rescaling of main parameters of Shuttle with regard to proposed LOX tank designs for SLS with 5 engines (the situation with 4 engines is less critical). Our investigations based both on theoretical analysis and on MNM and 3D ANSYS package simulations allow us to make the following conclusions.

1. Hazard analysis for LOx ET shows that the pressure control bandwidth remains almost the same for the SLS. The time-traces of SLS LOx tank ullage pressure and temperature were calculated after an appropriate rescaling of the relevant parameters. The rescaling takes into account the increase by factor 5/3 of the linear dimension of the tank compared to the tank of the Shuttle. The rescaled parameters include flows of hot He and GOx, and also initial volumes of ullage and liquid in the tank. The predicted time-traces of the ullage pressure are found to fall within the acceptance limits for both SLS LOx tank shapes.
2. The MNM can reproduce accurately the pressure during pre-press and blow down.
3. For the GHe and GOx flow rates and the initial ullage volume rescaled by 5/3 for the SLS LOX ET, no new hazards are found for the tank performance; the temperature stratification is more pronounced in the rescaled SLS tank. Such stratification occurs due to slow mixing of GOx/He gases: the heavy cold GOx localizes near the liquid surface and the injected hot light He accumulates near the tank top. The stratification is predicted theoretically and confirmed and scaled by the MNM and 3D simulations.
4. Parameters of the MNM, developed in our group, were fitted to make the MNM reproduce the ullage temperature stratification observed in the 3D simulations. Remarkably, it is found that an accurate correspondence between the model and the 3D simulations is achieved by fitting just a single parameter: the scale of the velocity of natural convection in the turbulent boundary layer near the tank wall.
5. The MNM reproduces with high accuracy the telemetric data of saw-tooth modulations of the ullage pressure during pre-pressurization stage, which result from injections of He pulses. This accuracy only required fitting the shape of the He pulses. Likewise, the model is found to reproduce fairly well the telemetric Shuttle data of the ullage pressure variation during the flight.

6. The ullage pressure in LOx tank is shown to be essentially insensitive to temperature stratification: a model calculation implies that even in the case of complete mixing of the cold and hot gases, where the temperature stratification is absent, the ullage pressure time-trace does not change significantly.

7. In contrast to the SLS LOx-shaped tank, the time-trace of the ullage pressure in SLS tank with LH2 shape is found to approach the lower acceptance limit. It is shown that this hazard can be eliminated by a decrease of the initial ullage volume in the tank.

8. Theoretical analysis of bubbles dynamics in LOx has been analyzed. It was shown that generated bubble volume increases as the tank height squared. Collapse of the bubbles during the early stage of the pre-pressurization has been demonstrated.

9. Condensation-evaporation flows are found to weakly affect the ullage pressure. First, the condensation is controlled by the high pressure of GOx in the ullage. In contrast to one's naïve expectations, even in a hypothetical case where the gas temperature in the vicinity of the liquid-vapor interface reaches the temperature of the injected He (320K) or GOx (800R=444K), it is condensation rather than evaporation which is dominant during the early pre-pressurization stage and the flight. In reality, due to stratification the actual temperature near the liquid-gas interface is much lower, which leads to strong suppression of evaporation during all stages of the pre-pressurization and the flight. Second, the condensation is controlled by the slow heat transfer rate in the LOx. It is predicted that the total condensed mass during the pre-pressurization and the flight is negligible. Therefore, large change of ullage pressure relating to condensation-evaporation process at the liquid-vapor interface is unlikely.

10. The estimated temperature of the interface is lower than 100K and the estimated thickness of the heated liquid layer is smaller than 1cm. This layer corresponds to the total mass of the heated liquid which is less than 450kg during the fight (t_{flight} =500sec). This mass is negligible compared to the total LOx mass in the filled tank, which is 627,500kg. Therefore, it does not play the role in the ullage temperature stratification and pressure dynamics. It was also found that the total heat associated with the condensation of GOx is much less than the heat of hot GOx injected during the flight.

11. Slight temperature stratification of LOx is formation of thin warm liquid layers with 90< T ≤ 98K near the interface and a layer with temperature T≤ 90.8K due to the liquid rising flow inside a very thin layer of thickness about 0.5mm. This liquid stratification does not play the role in the ullage temperature stratification and pressure dynamics and does not lead to breach of condition $NPSP = p_{ull} + p_{head} - p_{fric} - p_{s,vap}(T_s) > 30psi$ for the net positive suction pressure due to the high hydrostatic head pressure p_{head} near the feedline bottom.

12. Intensive longitudinal sloshing waves induced by the laterally excited rocket vibration change weakly the temperature liquid and ullage stratification and the ullage pressure during the flight. Maximum rate of condensation flow arising due to the strong mixing of the warm surface liquid layer with the cold deep layers is limited by value of $J_{cond}^{slosh} = 0.26\frac{kg}{\sec}$. The mass flow rate of injected hot GOx is much more $J_{GOx}(t) = 2.6\frac{kg}{\sec} \times (n_{nozzle}/3)$, n_{nozzle} is nozzle number in the SLS.

13. The vertical vibrations with the amplitude A_{vibr} and the frequency f_{vibr} such as $A_{vibr} > A_c = 0.1mm(100Hz/f_{vibr})^{2/3}$ induce generation of the warm droplets under the liquid-gas interface. Effect of axially excited vibration sloshing on LOx tank is extremely small as the temperature of generated warm droplets is very close to the interface temperature and condensation is depressed.

14. Combined action of intensive longitudinal and axial sloshing vibrations can induce relatively great condensation and formation of relatively thick hazard surface layer of heated liquid with temperature $T=T_s(p_{GOx})$. The rate of the condensation can reach $J_{drop}^{total} = 0.45kg/\sec$ and thickness, volume, and mass of surface heated hazard layer can

reach L_L=5cm, V=1.4m^3, and 1570kg, relatively. Total mass of LOX in the tank is 627,500kg$\times(n_{nozzle}/3)$.

15. A possible hazard is related to the increased length of the tank and the feed line joining LOx tank with the engines in the SLS. The height of the tank for SLS with 5 engines is about 25m and length of the feed line is about 50m. The hydrostatic head pressure near the bottoms of the tank and the feedline are 2.6amt and 9.2atm, respectively. The rocket acceleration during the fight reaches $2.5g_0$ causing the pressures to increase to 17atm and 29 atm, respectively. Such high hydrostatic pressures have to be taken into account in the process of manufacturing the feedline and the engine pumps with LOx propellant.

References

[1] External Tank, Propulsion Data Book, No. 80900200103, Lookheed Martin, 2005.

[2] "STS-115 ET-MPS Predicted Performance", Marshall Space Flight NASA Center Report, 4160/P-06-4011, August, 2006.

[3] L. Norquist, "External tank for the Space Shuttle Main Propulsion System", J. Spacecraft, 14, 358 (1977); G. M. Mactin, "A stratification prediction technique *for* cryogenic hydrogen and oxygen tanks under high-g conditions", October 1971, Summary Report, ASD-ASTN-1414, NASA MSF Center.

[4] P. N. Estey, D. H. Lewis Jr. and M. Connor, *Prediction of a Propellant Tank Pressure History Using State Space Methods*, J. of Spacecraft and Rockets, 20, pp. 49-54 (1983).

[5] Schallhorn, P., Campbell, D. M., Chase, S., Puquero, J., Fontenberry, C., Li, X., Grob, L., "Upper Stage Tank Thermodynamic Modeling Using SINDA/FLUINT", AIAA-2006-5051, 44rd AIAA/ASME/SAE/ ASEE Joint Propulsion Conference and Exhibit, Sacramento, CA, July 9-12, 2006

[6] V.V. Osipov, C.B. Muratov, "*Dynamic condensation blocking in cryogenic refueling*", Applied Physics Letters, 93, 224105 (2008).

[7]J. A. Clark, IAA/ASME/SAE/ASEE Joint Propulsion Conference and Exhibit,2004, unpublished, paper No. AIAA 2004-4088.

[8] V. V. Osipov, C. B. Muratov, E. Ponizovskaya-Devine, M. Foygel, and V. N. Smelyanskiy, "Cavitation-induced ignition of cryogenic hydrogen-oxygen fluids", APPLIED PHYSICS LETTERS **98**, 134102 (2011)

[9] M.D. Kannapel, A.J. Przekwas, A.K. Singhal and N.C. Costes. "Liquid Oxygen Sloshing in Space Shuttle External Tank", AIAA-87-201 1-9.

[10] J. Lacapere, B. Vieille, and B. Legrand, " Experimental and numerical results of sloshing with cryogenic fluids", Progress in Propulsion Physics, 1, 267-278 (2009).

[11] Baburaj, A. Puthenve Ettil and E. J. Hopfinger, "Evolution and breaking of parametrically forced capillary waves in a circular cylinder", Acepted to J. Fluid Mech. (2012).

[12]. M. E. Moran, N B. McNelis, M. T. Kudlac M. S. Haberbusch and G. A. Satornino. Experimental Results of Hydrogen Slosh in a 62 Cubic Foot (1750 Liter) Tank. AIAA-94-3259 (1994).

[13]. M.D. Kannapel, A.J. Przekwas, A.K. Singhal and N.C. Costes. Liquid Oxygen Sloshing in Space Shuttle External Tank, AIAA-87-201 1-9.

[14]. S. P. Das and E. J. Hopfinger. Parametrically forced gravity waves in a circular cylinder and finite-time singularity. J. Fluid Mech. (2008), vol. 599, pp. 205–228.

[15]. Baburaj, A. Puthenve ettil and E. J. Hopfinger. Evolution and breaking of parametrically forced capillary waves in a circular cylinder. J.Fluid Mech.

"Proceedings of the conference on propellant tank pressurization and stratification January 20, 1965, volume, NASA Marshall Space Flight Center.